Electrochemical, surface analysis, computational and anticorrosive studies of novel naphthalene derivative on carbon steel surface

E.H. Akroujai,[1] S. Chetioui,[2,3] N. Benzbiria,[4] A. Barrahi,[5] A. Chraka,[6] A. Djedouani,[7,8] S. Chtita,[9] B. Dikici,[10] I. Warad,[11] A. Bellaouchou,[5] M. Assouag[1] and A. Zarrouk[5]*

[1]Team of Innovative Materials and Mechanical Manufacturing Processes, ENSAM, University Moulay Ismail, B.P. 15290, Al Mansour, Meknes, Morocco
[2]Unité de Recherche de Chimie de l'Environnement et Moléculaire Structurale, (CHEMS), Faculté des Sciences Exactes, Département de Chimie, Université des Frères Mentouri, Constantine 1, Constantine 25000, Algérie
[3]Faculté de Technologie, Université Mohamed Boudiaf M'sila, Algérie
[4]Laboratory of Interface Materials and Environment, Faculty of Sciences Ain Chock, Hassan II University, B.P. 5366 Maârif, Casablanca, Morocco
[5]Laboratory of Materials, Nanotechnology, and Environment, Faculty of Sciences, Mohammed V University in Rabat, Morocco, PO. Box. 1014, Rabat, Morocco
[6]Materials and Interfacial Systems Laboratory, ERESI Team, Department of Chemistry, Faculty of Sciences, Abdelmalek Essaâdi University, Morocco
[7]Laboratoire de Physicochimie Analytique et Cristallochimie des Matériaux Organométalliques et Biomoléculaires, Université Constantine 1, 25000, Algérie
[8]Ecole Normale Supérieure de Constantine, Université Constantine 3, 25000, Algérie
[9]Laboratory of Analytical and Molecular Chemistry, Faculty of Sciences Ben M'Sik, Hassan II University of Casablanca, Morocco
[10]Ataturk University, Department of Mechanical Engineering, 25240 Erzurum, Turkey
[11]Department of Chemistry, AN-Najah National University, P.O. Box 7, Nablus, Palestine
**E-mail: azarrouk@gmail.com*

Abstract

In the present research, the inhibitive potency of (*E*)-1-(phenyldiazenyl)naphthalen-2-ol (EPNO) for carbon steel (CS) in molar HCl acid was investigated using potentiodynamic polarization (PDP) and electrochemical impedance spectroscopy (EIS). Based on the examination of Tafel data, it was revealed that EPNO displayed a mixed-type nature. EIS plots evinced that increasing the concentration of EPNO resulted in a significant 12-fold increase in polarization resistance (R_p) and a corresponding alteration in the double layer capacitance (C_{dl}) from 116.2 to 45.9 μF·cm^{-2}. The inclusion of 10^{-3} M of EPNO to the solution resulted in a maximum inhibition efficiency of 91.7%. Thermodynamic activation descriptors were also assessed as a function of EPNO concentration. The adsorption of EPNO on the CS substrate followed the Langmuir isotherm. The formation of a barrier layer was confirmed by scanning electron microscopy (SEM) coupled with energy-dispersive X-ray spectroscopy (EDX) and UV-Visible assays. Overall, the findings revealed that EPNO effectively provided an adequate

protection to CS and mitigated its corrosion. Finally, the theoretical studies based on the density functional theory (DFT), the molecular dynamics (MD) and the Monte Carlo (MC) simulations were also performed for understanding the adsorption mechanism of EPNO onto Fe-surface.

Received: September 24, 2023. Published: October 5, 2023 doi: 10.17675/2305-6894-2023-12-4-5

Keywords: *naphthalene, carbon steel, corrosion, PDP/EIS, SEM/EDX/UV-Visible, DFT/MC/MD.*

1. Introduction

Steel corrosion is a natural process that takes place when iron reacts with its surroundings in the presence of humidity and oxygen [1]. Corrosion phenomenon can occur in diverse environments such as industrial, marine and atmospheric conditions as well [2]. Several factors contribute to influence corrosion such as temperature, humidity, presence of pollutants and pH levels [3]. In fact, steel corrosion is accelerated in acidic media since acids have the ability to breakdown the protective oxide layer [4, 5]. The presence of hydrogen ions (H^+) increments the rate of electrochemical reactions, inducing thus the dissolution of iron ions and the formation of corrosion byproducts.

Regardless of steel response in acidic media, it remains one of the most utilized metal in various industries and environments [6, 7]. As a matter of a fact, steel is employed in the construction of pipelines, storage tanks, and reactors that handle corrosive acids, used in acid leaching operations to extract valuable metals from ores, and utilized in wastewater treatment plants where it comes into contact with acidic solutions [8, 9]. Other applications comprise acid pickling tanks, acid circulation systems, and acid scrubbers in the pharmaceutical industry [10].

In each of these usages, installing proper protection measures against corrosion is particularly crucial to ensure the maintenance of the structural integrity and longevity of steel components [11–13]. There are several methods available to combat steel corrosion in acidic media such as coating the steel with corrosion-resistant materials (epoxy, polyurethane or fluoropolymer), applying inhibitors, and implementing cathodic protection (connecting the steel to a sacrificial anode) [14–16]. The use of organic inhibitors involves the addition of the organic compounds to the solution or their direct application to the steel surface in order to form a protective film that prevents contact with the aggressive environment and mitigates thus corrosion process [17–19]. These inhibitors usually perform by adsorbing onto the metal surface and blocking the access of corrosive agents to steel surface even at low concentrations. Organic inhibitors are often preferred since they are non-toxic, cost-effective and ease of application [20]. The combination of organic inhibitors with other protective measures can provide a successful synergistic corrosion protection, further improving the longevity and performance of steel components in acidic media. In the literature, organic products [21–23] comprising electron rich centers as polar functional groups, double/triple links, aromatic ring (s) and/or side chain exhibited high anti-corrosive properties. Moreover,

the occurrence of specific atoms (O, N, S and P) or bonds (N=N, C=N, C=S, C=C, R–OH, *etc*.) in the molecular skeleton of an organic compound ensures a strong adhesion of the inhibitor to the metallic substrate [24–26].

The purpose of this work is to investigate the performance of (*E*)-1-(phenyldiazenyl)naphthalen-2-ol (EPNO) compound as corrosion inhibitor for carbon steel (CS) in 1 M HCl solution. Various techniques such as PDP, EIS and SEM/EDS and UV-Visible were employed to evaluate the inhibition efficiency (%EI) of EPNO. The temperature effect was studied using PDP plots, thermodynamic descriptors were assessed accordingly. Moreover, DFT, MC and MD were used to support the findings of the experiment.

2. Materials and Methods

2.1. Materials

The investigated C-steel metal bar elemental composition is as follows (wt.%); C (0.370), Si (0.230), Mn (0.680), Cr (0.077), S (0.016), Ti (0.011), Ni (0.059), Co (0.059), Cu (0.16), and Fe (remainder). Before being submerged in the solutions, the metal specimens are prepared by being polished under freshwater utilizing sand paper that has incrementally finer particle sizes ranging from 150 to 1200. Following a distilled water washing, acetone degreaser, and air handler drying, these samples were processed.

2.2. Chemicals

With no further refinement, all of the compounds by Sigma-Aldrich (Spain) were utilized as received. The structure of EPNO is shown in Figure 1.

In order to make molar HCl solutions, analytical commercial grade 37% HCl was diluted with twice-distilled water. The corrosion tests were conducted in a 1 M HCl solution devoid of the inhibitor and with a range concentration from 10^{-3} M to 10^{-6} M. The electrochemical measurements were conducted in an environment of normal air with no agitation.

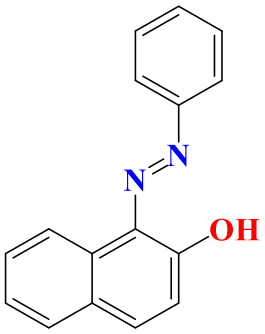

Figure 1. (*E*)-1-(phenyldiazenyl)naphthalen-2-ol (EPNO).

2.3. Electrochemical apparatus and measurements

A typical three-electrode cell is employed, consisting of a saturated calomel electrode (SCE) acting as a reference electrode, a platinum wire serving as the counter electrode (CE), and a steel working electrode (WE). To guarantee complete immersion of the electrodes in the cylindrical Pyrex glass cell, 90 cc of diluted hydrochloric acid were utilized. All studies were conducted at room temperature without stirring, with the exception of the impact temperature research.

Using a potentiostat Volta lab PGZ 100 and Voltamaster software, electrochemical measurements (Electrochemical Impedance Spectroscopy and potentiodynamic polarization curve measurements) were made. EIS and potentiodynamic curves were used to examine the corrosion behaviour of CS in a 1 M HCl solution in both the absence and presence of inhibitor solutions.

For 30 minutes, the working electrode was immersed in the test solution to create a stable open circuit potential (E_{OCP}). The electrochemical measurements were finished after E_{OCP} measurements. Plotting of the polarization curves was done at a scanning rate of $5 \cdot 10^{-4}$ V/s in the potential range of –0.8 V to –0.1 V/SCE. By recording the electrode potential ±0.01 V *versus* the open circuit potential starting at a higher negative potential, measurements of linear polarization resistance were made. The voltage has been stabilized for over 30 minutes prior to all testing. The electrochemical studies are triple-realized for each inhibitor concentration, and the best results are chosen for a graphical plot.

The following formula was used to compute the inhibitory efficiency (%):

$$\eta_{PP}(\%) = \frac{i_{corr} - i_{corr(inhib)}}{i_{corr}} \cdot 100 \quad (1)$$

i_{corr} and $i_{corr(inhib)}$ symbolize, respectively, the corrosion current densities in the presence and absence of inhibitive chemicals. For the temperature effect component, the operating temperatures range from 303 to 333 K.

Using the same workstation previously mentioned, the electrochemical impedance spectroscopy measurements were performed at open circuit potential using an AC signal with an amplitude of 10 mV and a frequency domain of 10^5 to 10^{-2} Hz. It was done by plotting the EIS diagrams using the Nyquist and Bode representations. The ZView software 3.4 software was then used to examine the results in terms of an equivalent electrical circuit.

The following formula was used to determine the inhibitory efficiency using EIS:

$$\eta_{EIS}(\%) = \frac{R_{P(inhib)} - R_P}{R_{P(inhib)}} \cdot 100 \quad (2)$$

with $R_{P(inhib)}$ and R_P indicate, respectively, the polarization resistance values in the presence and absence of the inhibitor.

We used the results of the blank for the stationary and transient polarisation techniques for the effect of temperature and concentration in the absence of the inhibitor EPNO, since we worked under the same conditions [27].

2.4. SEM explorations

SEM method has been used for surface examinations. The optimal concentration of 10^{-3} M corrosive solutions with and without inhibitive molecule was deployed. The samples were exposed to the aforementioned harsh mediums separately for 24 hours and removed delicately, rinsed with purified water, dried and then evaluated for surface morphological analysis using SEM. For the purpose of examining surface morphology, the JEOL-JSM-IT-100 model was utilized. The aforementioned metal was captured in 1000x magnification SEM pictures. We used the results of the blank in the absence and presence of HCl without inhibitor, since we worked under similar conditions in a work submitted simultaneously with this one.

2.5. UV-Vis. study

The absorption UV-visible spectroscopy technique has been used to investigate the inhibitor effectiveness against corrosion. It is based on their capacity to absorb light at specific wavelengths. In order to examine how organic molecules, interact with the metal surface in molar HCl solution, absorbance measurements of the solution have been carried out with and without C-steel sample being present in the acidic medium at the optimal concentration of 10^{-3} M. The wavelength scanning was done in the 200 to 600 nm range. A JASCO V-700 UV-Visible Spectrophotometer has been used.

2.6. Computational simulations details

Density Functional Theory (DFT) along with molecular simulations like molecular dynamics (MD) and Monte Carlo (MC) were employed in order to provide a deeper understanding of corrosion inhibitor molecules. These methods were used to uncover the characteristics and active sites of these molecules, as well as to investigate the process by which they attach to the surface of Fe-metal. This approach yielded intricate insights into the molecular-level mechanisms involved.

2.6.1. DFT simulation

To delve into the consistency between theoretical predictions and experimental observations, and to establish a connection between the projected inhibitory effectiveness of the investigated inhibitor (EPNO) and chemical reactivity indicators, the Density Functional Theory (DFT) approach was put to use, utilizing the Gaussian 09 software package [28]. The computations were conducted using the Becke, Lee–Yang–Parr (B3-LYP) functional [29, 30], and the 6-31G+(d, p) basis sets**.** Ground-state optimizations of the inhibitor's molecular structure in both aqueous and gaseous phases were carried out, followed by an

exploration of various electronic properties that correlated with these optimized parameters. These properties encompassed geometric attributes, as well as the characteristics of frontier molecular orbitals (E_{HOMO} and E_{LUMO}), and broader indicators of reactivity. By analyzing energy levels within the highest occupied molecular orbital (HOMO) and the lowest unoccupied molecular orbital (LUMO), a variety of chemical descriptors were computed. These included electron affinity (A), ionization potential (I), gap energy (ΔE), electronegativity (χ), and chemical hardness (η), all calculated using Equations 3–7 as previously reported [31–34]. Furthermore, the transition of electrons from occupied orbitals within the organic molecule to vacant orbitals on the metal surface (ΔN_{110}) was quantified using Equation 8. In this context, χ_{Fe} represented the work function (4.81 eV/mol) of the iron surface (Fe(110)), known for its heightened stabilization energy, while η_{Fe} denoted the absolute hardness of iron ($\eta_{Fe} = 0$ eV/mol) [35].

$$A = -E_{LUMO} \tag{3}$$

$$I = -E_{HOMO} \tag{4}$$

$$\eta = \frac{I - A}{2} \tag{5}$$

$$\Delta E = E_{LUMO} - E_{HOMO} \tag{6}$$

$$\chi = \frac{I + A}{2} \tag{7}$$

$$\Delta N_{110} = \frac{\chi_{Fe} - \chi_{inhibitor}}{2(\eta_{Fe} + \eta_{inhibitor})} \tag{8}$$

The distribution of frontier molecular orbitals (FMOs) and the Molecular Electrostatic Potential (MEP) map were also performed [32].

2.6.2. Molecular dynamics (MD) and Monte Carlo (MC) simulation approaches

Making use of molecular simulations, such as molecular dynamics (MD) and Monte Carlo (MC) the interaction of title molecule (EPNO) in its neutral and protonated form (*i.e.*, EPNO/EPNOH$^+$) onto Fe-substrate was investigated using Material Studio 8.0 software from the BIOVIA company. According to earlier reports for the representation of carbon steel, Fe (110) surface was adopted [36, 37]. To simulate the aqueous phase, like the experimental situation, MC and MD simulation was done in the presence of solvent molecules (*i.e.*, 1000 water (H_2O), 10 corrosive hydroniums (H_3O^+), and 10 chlorides (Cl^-) ions), as well as the EPNO/EPNOH$^+$ structures. The interactions EPNO/EPNOH$^+$–iron (Fe) substrate in the simulated corrosion media performed *via* the Fe(110) supercell of size (14×14) and a vacuum slab with (60 Å) thickness in a simulation box (34 Å×34 Å×68 Å) [38]. The potential energy values required for molecular interactions were derived from the COMPASS force field during both MC and MD simulations [39]. This force field, which

successfully predicts various gas-condensed-phase properties of a variety of compounds, has previously been used in investigations of inorganic and organic systems [40–42]. furthermore, MC calculations were performed using five cycles (15000 steps each cycle) of simulated annealing at 303 K. Furthermore, MD was achieved using an NVT canonical ensemble at 303 kelvin, 1 fs time step, and 800 picoseconds simulation period.

3. Results and Discussion

3.1. Electrochemical techniques

3.1.1. PDP results

The examination of PDP curves provides valuable insights into the electrochemical processes occurring on carbon steel in 1 M HCl in absence and presence of various EPNO concentrations. As depicted in Figure 2, both anodic and cathodic current densities undergo a substantial subsidence, which underscores the weakening of CS anodic dissolution as well as the generation of H2 in the studied medium. From the analysis of PDP plots, it can be noticed that the addition of EPNO to the aggressive solution does not affect the mechanism of H+ reduction as the cathodic branches present Tafel lines. Thus, for all studied concentrations, H+ reduction occurs mainly *via* electron transfer process [43]. Based on the scrutiny of anodic curves, two distinctive Tafel slopes may be observed (β_{a1} and β_{a2}). First of all, the anodic current densities increase as the potential is swiped towards more anodic values. Then, a pronounced escalation of anodic current densities is noticed at the point of reaching the desorption potential (E_{dsp}). Afterwards, the current density shows a flat trend for more anodic potentials. The observed conduct may be an indication of the displacement of the adsorption-desorption equilibrium towards EPNO desorption from CS substrate [44].

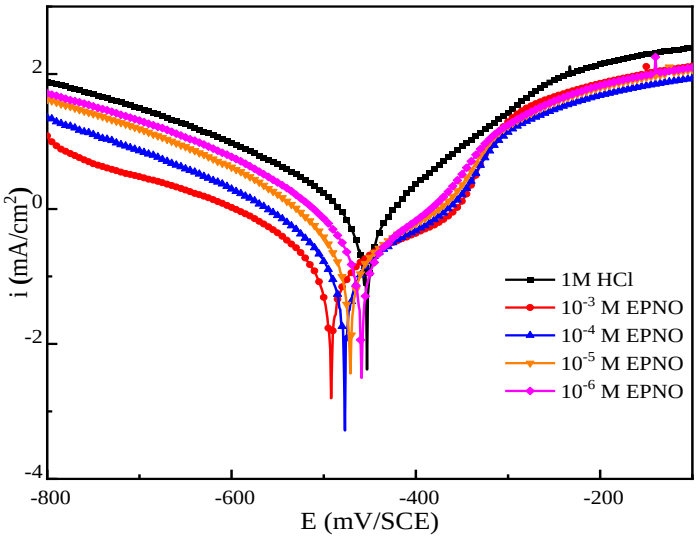

Figure . PDP plots for carbon steel in 1 M HCl in the absence and in the presence of diverse concentrations of EPNO.

The data in Table 1 highlights a gradual decline of i_{corr} values as EPNO concentration rises in 1 M HCl solution, as well as a shift of the potential of corrosion (E_{corr}) values to more negative values. Since the shift in E_{corr} is less than 85 mV compared to the blank test solution ($\Delta E_{corr} = 32.6$ mV for the system {CS/1 M HCl/10^{-3} M EPNO}), EPNO can be described as a mixed type inhibitor according to Riggs assertion [45–48].

Using Eq. (1), the inhibition activities η_{PP}(%) were assessed from PDP data and gathered in Table 1. The values η_{PP}(%) increase notably as EPNO concentration increases in the medium, attaining the highest value of $\eta_{PP} = 91.2\%$ for an optimal concentration of 10^{-3} M. The abovementioned outcomes additionally substantiate that the EPNO on Fe-CS/1 M HCl system shows promise to proficiently obstruct the active centers on CS and thereby impede corrosion.

Table 1. Potentiodynamic polarization descriptors for carbon steel in 1 M HCl without and with various EPNO concentrations at 303 K.

Medium	**Conc. (M)**	**$-E_{corr}$ (mV *vs.* SCE)**	**i_{corr} ($\mu A \cdot cm^{-2}$)**	**η_{pp} (%)**
Blank solution	1 M	456.3	1104	–
EPNO	10^{-3}	488.9	97.1	91.2
	10^{-4}	477.3	114.1	89.7
	10^{-5}	470.3	178.0	83.6
	10^{-6}	458.8	317.2	71.3

3.1.2. EIS data

EIS measurements were drawn for CS in contact of 1 M HCl with and without varying EPNO concentrations to evaluate the compound inhibitive potency, to additionally provide insights into corrosion phenomenon and investigate the reaction mechanisms occurring at the electrochemical interface. Figure 3 depicts the Nyquist representation of EIS data for CS in 1 M HCl at 303 K in presence and absence of EPNO. The progressive inclusion of EPNO to the test media results in a notable increment of the radius of the capacitive loops as opposed to the reference solution. Though, despite increasing EPNO concentration, the overall attribute of the loops remains unaltered. Such trend is emblematic of a corrosion phenomenon driven by a single electron transfer [49]. The depressed feature of the capacitive loops is indicative of multiple inputs such as surface coarseness, crystal lattice irregularities, porous structure, impurities and the spatial arrangement of active sites [50, 51].

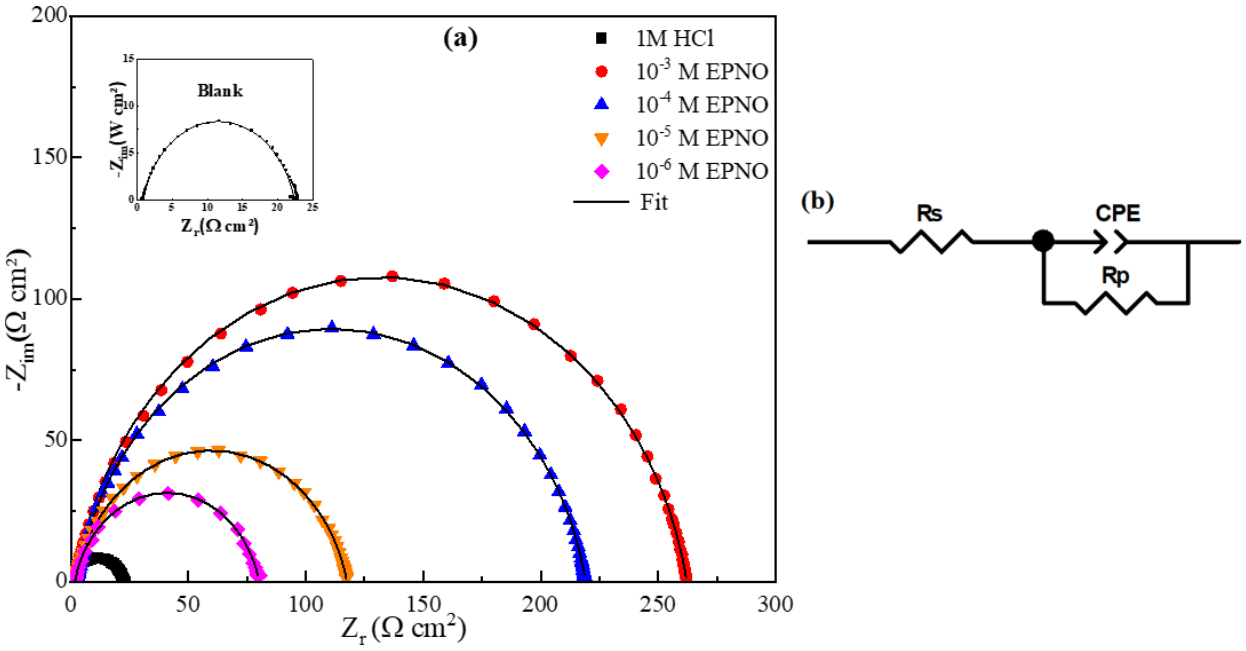

Figure 3. Nyquist diagrams of carbon steel in inhibitor free 1 M HCl solution and with the addition of various concentrations of EPNO at 303 K and (b) the corresponding electrical circuit employed for fitting EIS spectra.

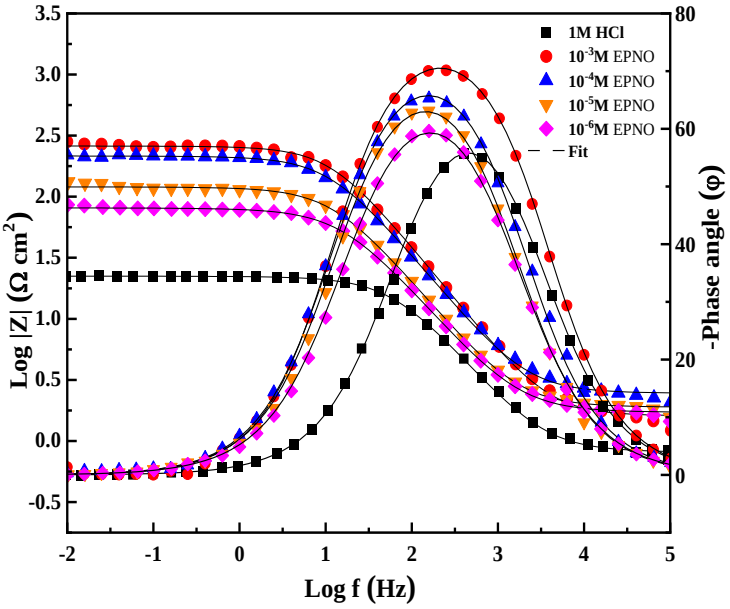

Figure 4. Bode's plots and phase at 303 K for carbon steel in 1 M HCl solution in the absence and presence of various concentrations of EPNO.

Figure 4 depicts the Bode representation of EIS data collected for CS in 1 M HCl with and without varying concentrations of EPNO. The plots are indicative of the presence of a unique capacitive time constant as well. It can be noticed that log|*Z*| and phase angle (θ) values approach zero in the high frequency range, which is indicative of the resistive conduct of the electrolyte's resistance. As for midrange frequencies, log|*Z*| and log*f* exhibit a linear

relationship having a slope below –1 and a θ inferior –90°. For an ideal system, a pure capacitor gives rise to a unitary slope of –1 and a θ of –90°. However, in our case, the deviation may be ascribed to the gradual deceleration of the dissolution rate over time [52]. Lastly, within the low frequency range, there is an enhancement of the resistive conduct of CS electrode as indicated by the independence of log|*Z*| of the frequency [53].

The electrical equivalent circuit (EEC) illustrated in Figure 3b encloses a solution resistance R_s, a polarization resistance R_p, and a Constant Phase Element (*CPE*) that portrays the double-layer capacitance (C_{dl}). In the electrical circuit, the *CPE* was incorporated instead of a pure capacitor to correctly match the EIS curves and better scrutinize the electrochemical processes interfering at the interface CS/EPNO/HCl [54]. The impedance function of a *CPE* is described by Equation 9:

$$Z_{CPE} = Q^{-1}(i\omega)^{-n} \tag{9}$$

where Q, i, ω, and n denote respectively the CPE constant, imaginary number ($i^2 = -1$), angular frequency ($\omega = 2\pi f$), and phase shift. n designates the divergence with respect to the ideal conduct, comprised between 0 and 1. Based on Macdonald *et al*. assertion [55], the value of n proffers an insight on the substrate heterogeneity. For instance, n is homologous to a resistance when $n = 0$, a capacitor for $n = 1$, and assigned to a diffusion process in case $n = 0.5$.

From *CPE* parameters, C_{dl} values were assessed according to Equation 10:

$$C_{dl} = (Q \cdot R_p^{1-n})^{-n} \tag{10}$$

Table 2 includes the main EIS descriptors (R_p, n, C_{dl}) derived from fitting of impedance data. The acquired parameters highlight that the value of R_p is enhanced with EPNO concentration. For instance, the presence of 10^{-3} M of EPNO raises R_p 12 times contrasted with the reference solution. This observation may be attributed to a sluggish corrosion process resulting from a deficiency in active centers where the reaction may take place. The inhibition potency η_{EIS}(%) of ENPO was assessed from the values of R_p through Equation 2. As shown in Table 2, the estimated η_{EIS}(%) reaches a maximal value of 91.7% for a concentration of 10^{-3} M of EPNO. Further examination of Table 2 points out to a noteworthy decline of C_{dl}, expressly the values dropped from 116.2 in the blank test solution to 45.9 μF·cm^{-2} in presence of 10^{-3} M EPNO. This decline is attributed to a subsidence of local dielectric constant and/or increment of double layer thickness. Furthermore, a slight increment of n values from 0.845 to 0.88 is noticed after adding of 10^{-3} M of EPNO to the solution, revealing that the surface heterogeneity moderately reduces as a result of adsorption of the inhibitory molecules. In alternative terms, one can assume that EPNO molecules have great inhibitive potential. The molecules adsorb on carbon steel surface, eradicate the initial components and diminish the number of active sites commonly implicated in the corroding of CS in HCl solution [56].

Table 2. Electrochemical impedance descriptors of carbon steel in 1 M HCl solution comprising varied concentrations of EPNO at 303 K.

Medium	C (M)	R_s ($\Omega \cdot cm^2$)	R_P ($\Omega \cdot cm^2$)	C_{dl} ($\mu F \cdot cm^{-2}$)	$10^6 \times A$ ($\Omega^{-1} s^n \cdot cm^{-2}$)	n_{dl}	χ^2	η_{EIS} %
HCl	1M	0.83	21.57	116.2	293.9	0.845	0.002	–
EPNO	10^{-3}	1.6	260.5	45.9	78.1	0.880	0.008	91.7
	10^{-4}	1.4	216.4	56.4	100.0	0.873	0.009	90.0
	10^{-5}	1.9	115.6	86.2	154.1	0.874	0.008	81.3
	10^{-6}	1.8	75.4	94.7	180.0	0.870	0.009	71.4

3.2. Effect of temperature

Many researchers reported significant alteration of metals conduct by temperature in aggressive media, as well as the impact noticed on the interaction between the substrate and the inhibitory compounds. Therefore, the evaluation of the influence of temperature on EPNO inhibitive potency was studied through PDP curves after immersion of CS electrode in 1 M HCl with and without 10^{-3} M EPNO at temperatures in the range of 303–333 K (Figure 5 and 6). Table 3 gathers the electrochemical descriptors derived from PDP curves. The increase of temperature leads to a rise of i_{corr} values in both the reference solution and in the presence of EPNO inhibitor, resulting systematically to a subsidence of η_{PP}% values. In previous studies, it was revealed that the interaction of the inhibitory molecules and the metallic substrate was negatively affected by the increase of temperature, as the coarseness of metallic surfaces increases at higher temperatures [57, 58]. From these observations, one may suggest that the chemical performance of EPNO molecules is depleted as the temperature raises, inducing a partial desorption of EPNO from CS surface [59]. It is interesting to mention that EPNO still exhibits good values of η_{PP}% in the inspected temperatures (η_{PP}% = 84.4% at 333 K).

Activation thermodynamic descriptors such as E_a (activation energy), ΔH_a^* (activation enthalpy) and ΔS_a^* (activation entropy) were determined by examining the temperature influence as designated by the Arrhenius law (Equation 11) and transition state formula (Equation 12) [60]:

$$i_{corr} = A\exp\left(\frac{-E_a}{RT}\right) \tag{11}$$

$$i_{corr} = \frac{RT}{Nh}\exp\left(\frac{\Delta S_a^*}{R}\right)\exp\left(\frac{-\Delta H_a^*}{RT}\right) \tag{12}$$

where A denotes the Arrhenius constant, R designates the gas constant, T represents the absolute temperature (K), N denotes the Avogadro's number and h stands for the Planck's constant.

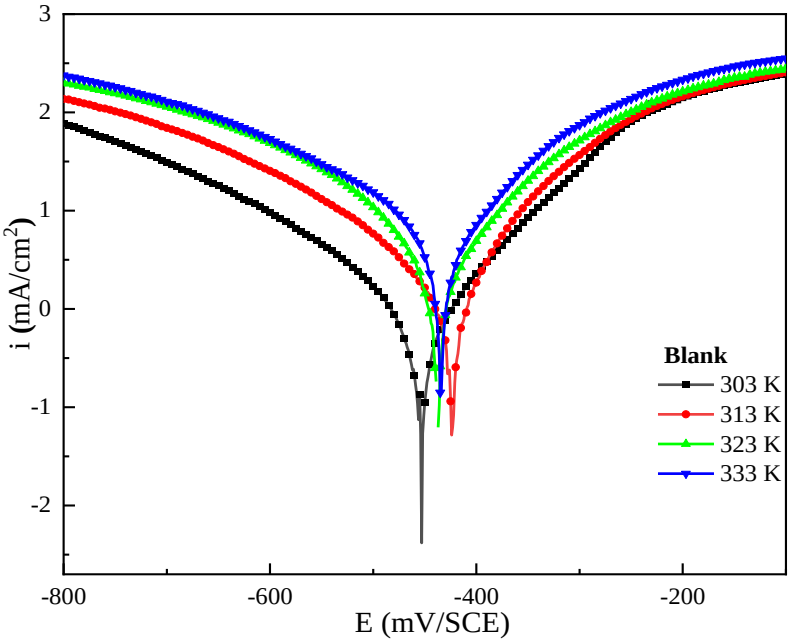

Figure 5. Potentiodynamic polarization curves for carbon steel in the absence of EPNO inhibitor at different temperatures from 303 K to 333 K.

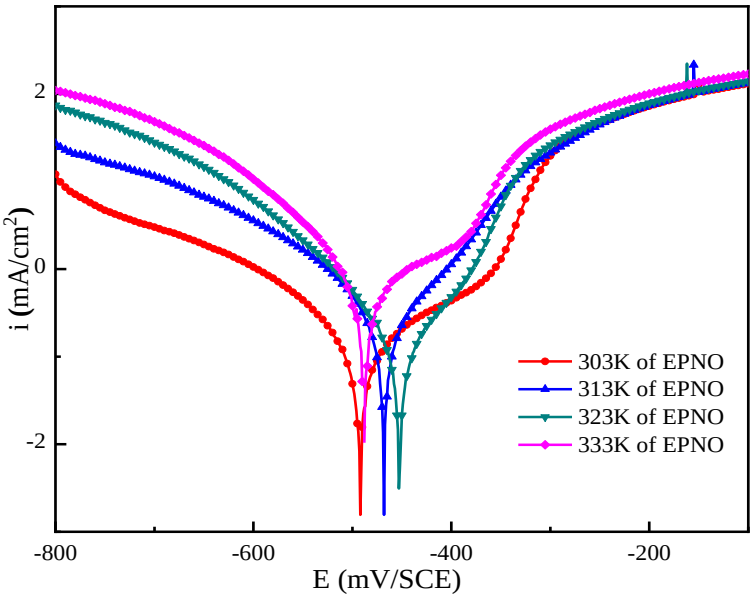

Figure 6. Potentiodynamic polarization curves for carbon steel in the present of 10^{-3} M of EPNO at different temperatures from 303 K to 333 K.

Table 3. PDP parameters for carbon steel in the present of 10^{-3} M of the blank and inhibitor at different temperatures between 303 K–333 K.

Medium	Temp. K	$-E_{corr}$ mV/SCE	i_{corr} μA·cm^{-2}	η_{PP}, %
Blank	303	456.3	1104.1	–
	313	423.5	1477.4	–
	323	436.3	2254.0	–
	333	433.3	3944.9	–
EPNO	303	488.9	97.1	91.2
	313	468.4	167.3	88.7
	323	451.8	298.4	86.8
	333	485.9	616.1	84.4

The respective plots are depicted in Figure 7 and Figure 8. As depicted in Figure 7, the Arrhenius plotting exhibits straight lines whose slopes are equal to $-E_a/R$. From Table 4, it can be noted that the determined value of E_a for CS in 1 M HCl including the inhibitor EPNO (51.2 kJ/mol) is greater with respect to the reference solution (35.4 kJ/mol). Thus, it can be suggested that the energy barrier corresponding to the corroding process enhances with adding EPNO to the studied medium. As a result, corrosion will turn into a more difficult and challenging process on the substrate which is accounted to the obstruction of CS active centres by EPNO molecules [58].

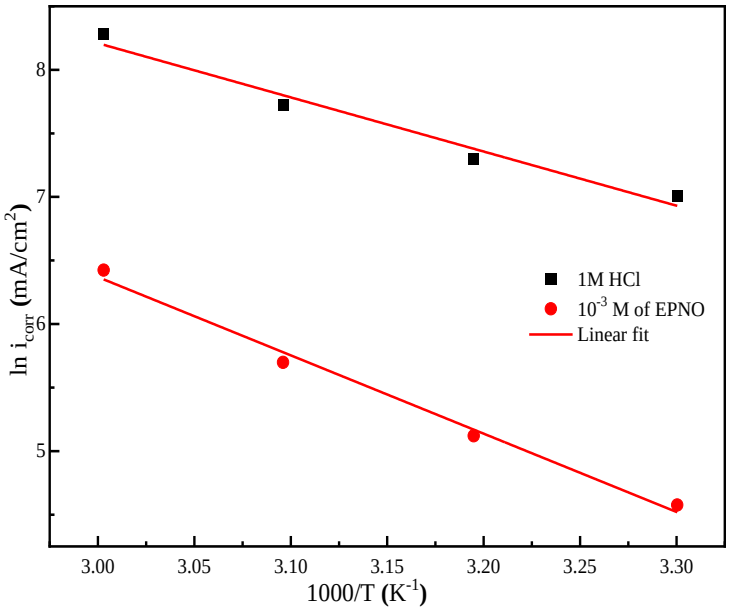

Figure 7. Arrhenius graphs for carbon steel in 1 M HCl without and with 10^{-3} M of EPNO.

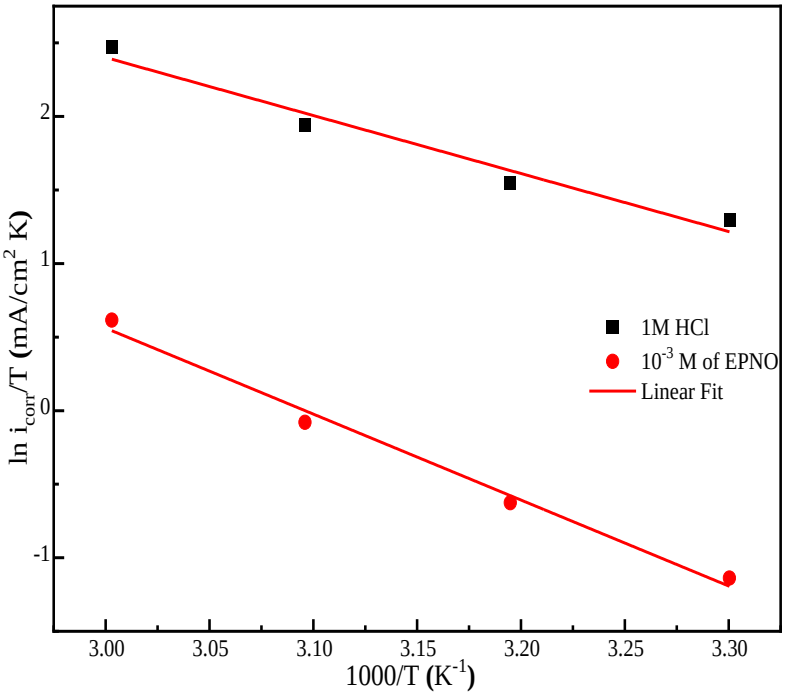

Figure 8. Transition Arrhenius plots of carbon steel in 1 M HCl with and without 10^{-3} M of EPNO.

Furthermore, the analysis of Table 4 indicates that the generation of the activated complex can be considered as an endothermic process since $\Delta H_a^* > 0$. Note that ΔH_a^* value is higher with adding EPNO to the solution. This can be an indication that the corroding process of CS is mitigated by EPNO molecules. The positive increase of ΔS_a^* following the addition of EPNO demonstrates that the transformation of reactants to activated complexes generates an increment in the reaction's disorder [61].

Table 4. Activation parameters generated in 1 M HCl without and with 10^{-3} M EPNO.

Medium	E_a, **(kJ/mol)**	$-\Delta H_a^*$, **(kJ/mol)**	ΔS_a^*, **(J/mol·K)**
Blank	35.4	32.8	–79.2
EPNO	51.2	56.9	–47.1

3.3. Adsorption isotherm

Researchers revealed in earlier studies that the interaction of organic products with metals may be considered as a quasi-replacement of water molecules by organic molecules ($Org_{(aq)}$) as expressed by the following reaction:

$$Org_{(aq)} + xH_2O_{(ads)} \rightarrow Org_{(ads)} + xH_2O_{(aq)} \quad (13)$$

where *x* stands for the number of H_2O molecules expelled by the adsorbed inhibitors on the metallic surface.

Generally, isotherms are practical tools used to provide valuable insights on the adsorption capacity, affinity and mechanisms of inhibitors on metals. To this end, various types of isotherms (Langmuir, Freundlich, and Temkin) were plotted in attempt to model the adsorption process and extract relevant information. As presented in Figure 9, the Langmuir model is the most appropriate isotherm to describe the adsorption process, as it exhibits an almost unitary correlation. The Langmuir isotherm formula relates the fractional surface coverage (θ) to the equilibrium concentration of the inhibitor (*C*) as given by Equation 14 [62, 63]:

$$\frac{C}{\theta} = \frac{1}{K_{ads}} + C \tag{14}$$

where K_{ads} denotes the adsorption/desorption equilibrium constant and *C* stands for EPNO concentration in the medium.

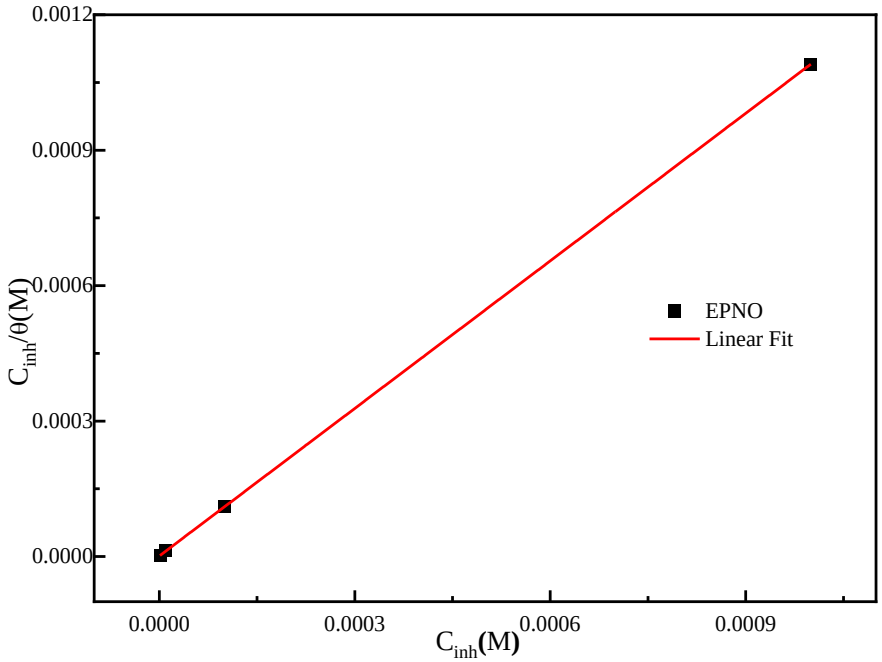

Figure 9. Langmuir adsorption isotherm plots for carbon steel in 1 M HCl in the presence of EPNO.

In accordance to Table 5, the high value of K_{ads} emphasizes the adsorption potency of the inhibitor EPNO. Therefore, it can be assumed that EPNO is adsorbed on a homogenous surface having a limited number of adsorption sites. This model also indicates that EPNO molecules formed a monolayer on CS surface with no interaction between the adsorbed molecules.

The values of the standard adsorption free energy (ΔG_{ads}) were assessed by using Equation 15 [61]:

$$\Delta G_{ads} = -RT\ln(55.5K) \quad (15)$$

where R designates the gas constant and T stands for the absolute temperature (K). The 55.5 value designates H_2O concentration in the solution (mol/L).

From exploring the experimental data fitted to the Langmuir equation, the derived value of ΔG_{ads} ($\Delta G_{ads} = -44.3$ kJ/mol) points out that the EPNO layers adsorbed on CS surface are stable [61]. As ΔG_{ads} value is close to –40 kJ/mol, it may be assumed that a covalent bond is formed (chemical adsorption) *via* charge transfer between EPNO and CS surface [64].

Table 5. Thermodynamic parameters for corrosion of carbon steel in 1 M HCl in the presence of EPNO.

Inhibitor	K_{ads}, (L/mol)	ΔG_{ads}, (kJ/mol)	Slope	R^2
EPNO	788618.7	–44.3	1.1	1

3.4. SEM/EDX analysis

In order to assess carbon steel behavior and examine its surface morphology, SEM/EDX analysis was conducted in 1 M HCl after 24 h immersion at 303 K in absence and presence of 10^{-3}M of EPNO. The micrograph collected for sanded CS depicts few scratches with no discernable defects (Figure 10a). When exposed to the acidic environment (Figure 10b), CS undergoes vigorous attack, involving corrosion products as evidenced by the development of a finely patterned rust layer. The related EDX analysis depicts corrosion products elements such as Cl and O atoms, pointing out to the possible formation of $FeCl_2$ and Fe_3O_4 [65]. After inhibition by EPNO, the surface morphology of CS exhibits discernible alteration (Figure 10c). SEM analysis presents a smoother surface as opposed to the corroded one. Besides, the development of corrosion byproducts, commonly observed in acidic media, noticeably subsided and even eradicated. As shown in Figure 10c, EPNO compound formed a cohesive and uniform barrier layer against corrosive agents. The presence of EPNO is entailed *via* EDX analysis depicting the occurrence of O and N atoms. It is also worth to mention that the intensity of Cl peaks significantly decreases. Overall, one may assume that EPNO adsorbed on CS surface and altered its morphology, enhanced corrosion resistance and preserved the integrity of CS specimen through the formation of a stable and adherent protective film.

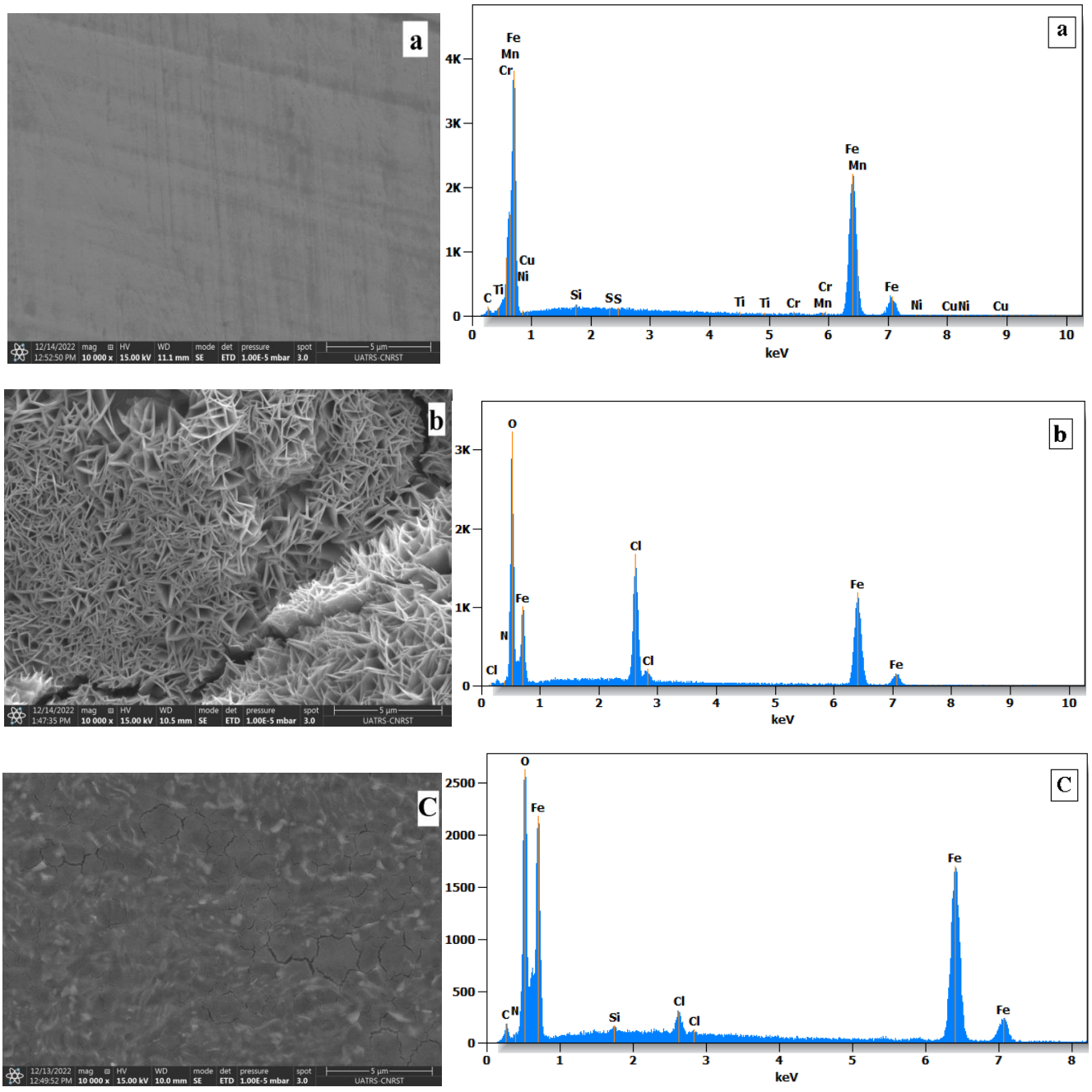

Figure 10. SEM/EDX analysis of carbon steel specimens (a) before immersion, (b) after 24 h immersion in 1 M HCl and (c) 1 M HCl + 10^{-3} M of EPNO at 303 K.

3.5. UV-Visible Study

UV-Visible trials were performed to assess the interaction of CS surface and EPNO molecules 1 M HCl solution enclosing 10^{-3} M of EPNO before and after immersion of CS for 72 h at 303 K (Figure 11). Before the immersion of CS (black curve), a distinctive single absorbance band is depicted around 331.4 nm. Whereas, after CS immersion (red curve), the wavelength value is displaced towards 224.8 nm. The changes in the absorbance of light in the UV-Visible spectrum indicate the formation of a complex between Fe^{2+} ions and EPNO

molecules in 1 M HCl [66, 67]. The UV-Vis outcomes further confirm the alteration of CS surface *via* the adsorption of EPNO compound.

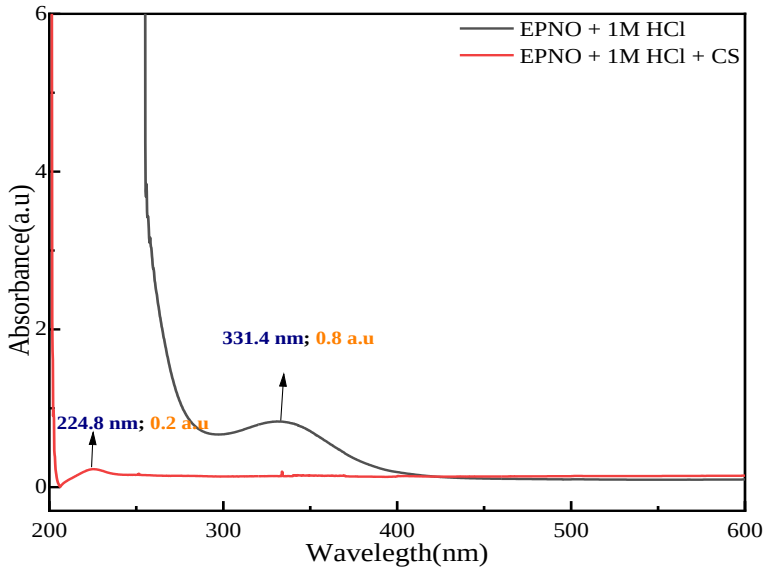

Figure 11. UV-Vis spectra of EPNO inhibitor solution before and after 3 days of immersion in 1 M HCl.

3.6. Molecular simulations

3.6.1. Protonation forms

In an acidic solution, the likelihood of protonation is significant when an organic molecule containing heteroatoms is present. Figure 12 illustrates four distinct protonation forms and the corresponding electronic distribution within the EPNO structure. Notably, form A emphasizes that the two nitrogen atoms are the most favorable sites for proton (H^+) attachment. This protonation event can potentially alter the molecule's chemical reactivity while also facilitating the establishment of electrostatic bonds with chloride ions that are adsorbed on the surface of the steel.

(a)

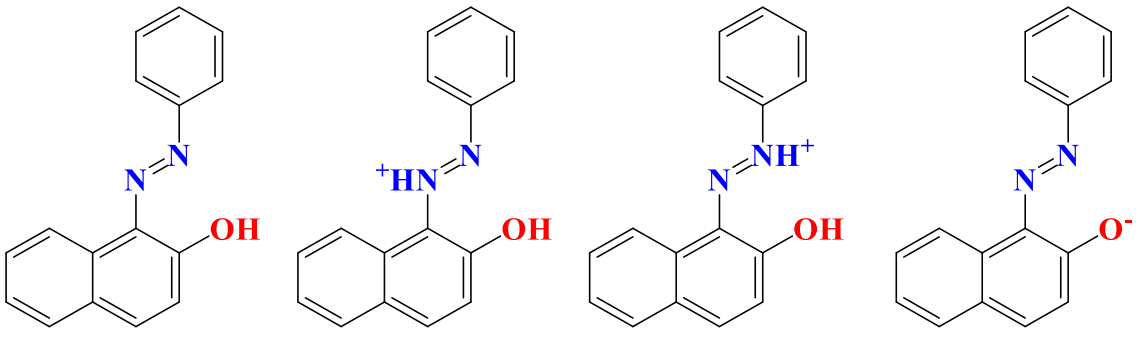

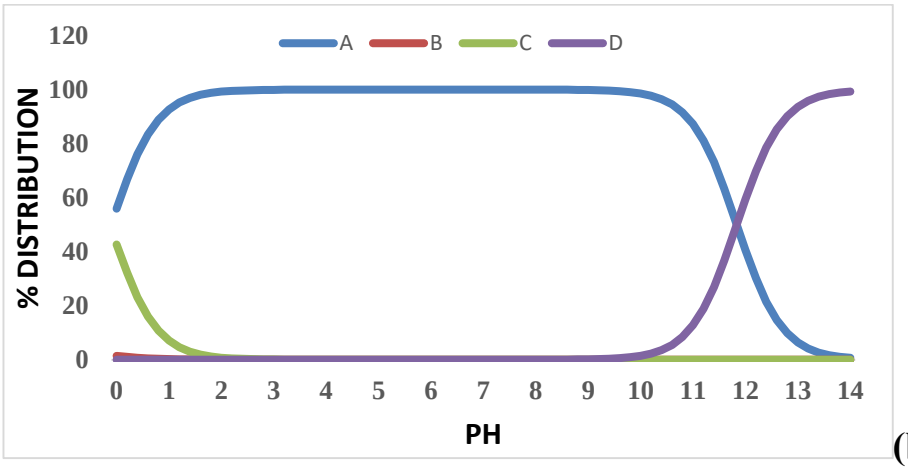

(b)

Figure 12. (a) Different protonation forms of the EPNO; (b) Electronic distribution within the EPNO.

3.6.2. Density functional theory (DFT) approaches

3.6.2.1. Optimized structure

DFT has indeed demonstrated significant utility in determining molecular structures, electronic attributes, and molecular reactivity. With impressive progress in supercomputing capabilities, the effectiveness of this method has been further enhanced. Experimental techniques utilized for studying corrosion inhibition and comprehending its mechanisms can be resource-intensive and time-consuming. Consequently, theoretical calculations leveraging DFT have been leveraged to clarify the interactions between inhibitor molecules and Fe-surface, offering valuable insights into the mechanisms of inhibition. Figure 13 illustrates the optimized molecular structure of EPNO, featuring labeled atoms and numbering. Moreover, Table 6 presents the optimized molecular geometric parameters, such as bond lengths and angles computed using the B3LYP/6-31+G(d,p) level of theory.

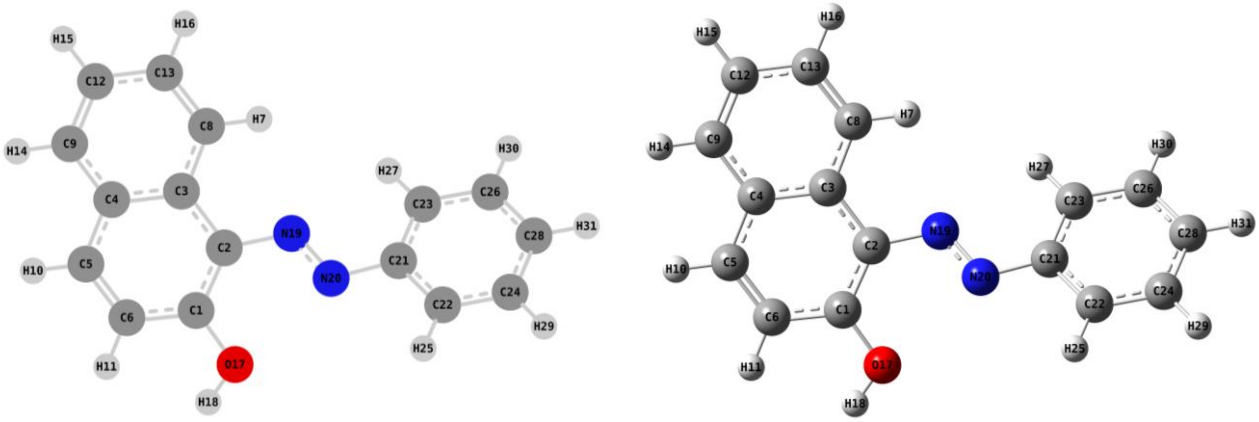

Figure 13. Optimized structure of the EPNO at the B3LYP/6-31+G(d,p) level.

Table 6. Optimized geometric parameters of the EPNO in aqueous and gas phases.

Lengths	Aqueous	Gas	Angles	Aqueous	Gas	Angles	Aqueous	Gas
R(1,2)	1.4050	1.4026	A(2,1,6)	120.2787	120.1149	A(20,21,22)	115.4827	115.3450
R(1,6)	1.4185	1.4182	A(2,1,17)	120.3222	120.3630	A(20,21,23)	124.7332	124.7838
R(1,17)	1.3592	1.3609	A(6,1,17)	119.3660	119.4900	A(22,21,23)	119.7742	119.8602
R(2,3)	1.4458	1.4427	A(1,2,3)	118.8993	118.9791	A(21,22,24)	120.2380	120.1881
R(2,19)	1.4016	1.4040	A(1,2,19)	125.9981	125.5862	A(21,22,25)	118.7518	118.3275
R(3,4)	1.4313	1.4313	A(3,2,19)	114.9243	115.2552	A(24,22,25)	121.0089	121.4837
R(3,8)	1.4222	1.4219	A(2,3,4)	119.8934	120.0200	A(21,23,26)	119.6585	119.6202
R(4,5)	1.4216	1.4199	A(2,3,8)	122.0116	121.8261	A(21,23,27)	119.4348	119.1586
R(4,9)	1.4214	1.4210	A(4,3,8)	118.0899	118.1494	A(26,23,27)	120.9052	121.2194
R(5,6)	1.3734	1.3737	A(3,4,5)	118.8178	118.7361	A(22,24,28)	119.9452	119.9411
R(5,10)	1.0862	1.0866	A(3,4,9)	119.7372	119.6548	A(22,24,29)	119.8674	119.9098
R(6,11)	1.0871	1.0884	A(5,4,9)	121.4446	121.6087	A(28,24,29)	120.1868	120.1484
R(7,8)	1.0830	1.0828	A(4,5,6)	120.9669	120.8389	A(23,26,28)	120.4845	120.4665
R(8,13)	1.3819	1.3802	A(4,5,10)	119.2140	119.2163	A(23,26,30)	119.6681	119.7102
R(9,12)	1.3792	1.3778	A(6,5,10)	119.8189	119.9448	A(28,26,30)	119.8464	119.8224
R(9,14)	1.0868	1.0871	A(1,6,5)	121.1307	121.2984	A(24,28,26)	119.8906	119.9145
R(12,13)	1.4156	1.4155	A(1,6,11)	118.5871	118.5436	A(24,28,31)	120.1209	120.1110
R(12,15)	1.0857	1.0859	A(5,6,11)	120.2820	120.1567	A(26,28,31)	119.9868	119.9727
R(13,16)	1.0862	1.0864	A(3,8,7)	118.8731	118.5995	–	–	–
R(17,18)	0.9692	0.9673	A(3,8,13)	120.8811	120.8432	–	–	–
R(19,20)	1.2639	1.2617	A(7,8,13)	120.2458	120.5573	–	–	–
R(20,21)	1.4211	1.4197	A(4,9,12)	120.8171	120.8370	–	–	–
R(21,22)	1.4040	1.4027	A(4,9,14)	118.6004	118.6175	–	–	–
R(21,23)	1.4080	1.4069	A(12,9,14)	120.5825	120.5455	–	–	–
R(22,24)	1.3963	1.3955	A(9,12,13)	119.5892	119.6187	–	–	–
R(22,25)	1.0858	1.0855	A(9,12,15)	120.3828	120.3540	–	–	–
R(23,26)	1.3929	1.3921	A(13,12,15)	120.0280	120.0273	–	–	–
R(23,27)	1.0840	1.0841	A(8,13,12)	120.8841	120.8958	–	–	–
R(24,28)	1.3984	1.3977	A(8,13,16)	119.5204	119.5326	–	–	–
R(24,29)	1.0858	1.0861	A(12,13,16)	119.5952	119.5713	–	–	–
R(26,28)	1.4029	1.4021	A(1,17,18)	109.3959	109.0247	–	–	–
R(26,30)	1.0862	1.0865	A(2,19,20)	118.1245	117.2266	–	–	–
R(28,31)	1.0859	1.0862	A(19,20,21)	114.4981	114.4738	–	–	–

3.6.2.2. Frontier molecular orbitals

Figures 14 and 15 present the frontier molecular orbitals (FMO), specifically highlighting the Highest Occupied Molecular Orbital (HOMO) and the Lowest Unoccupied Molecular Orbital (LUMO), alongside the molecular electrostatic potential (MEP) of EPNO. These figures offer a depiction of the three-dimensional molecular structures in their most stable configurations, devoid of any observed negative frequencies. The electron density distribution across these optimized structures is effectively illustrated by the HOMO and LUMO representations. Examining Figure 14, it becomes evident that both LUMO and HOMO exhibit electron densities that extend throughout the entirety of the neutral molecule. This observation suggests the presence of electron acceptors distributed across atoms and heteroatoms within the structure. Furthermore, this suggests that the EPNO structure could potentially interact with the studied metallic support through coordination bonds, as well as establish electrostatic bonds, indicating its versatile adsorption potential.

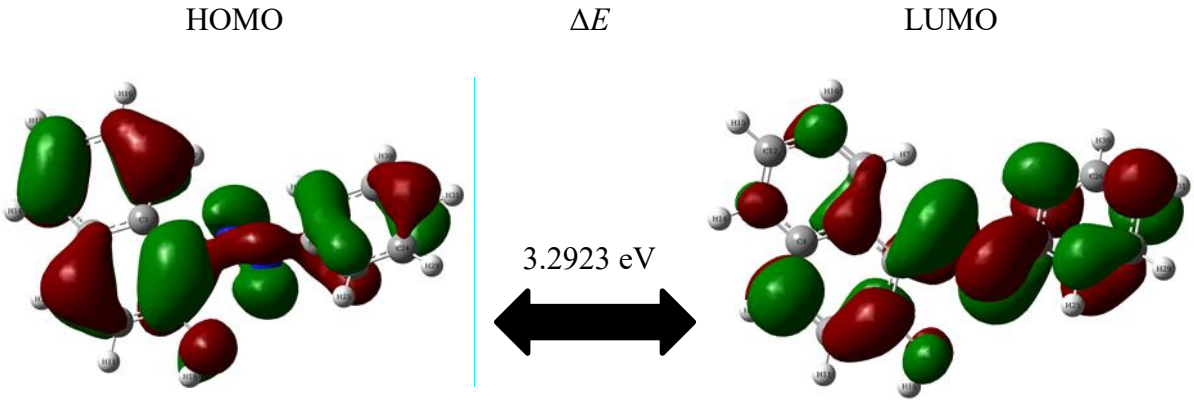

Figure 14. The contour plots of FMO for the investigated inhibitor (EPNO).

Conducting MEP investigations offers valuable information about the electrophilic and nucleophilic sites within the studied inhibitor, allowing for predictive analysis of reactive regions. As shown in Figure 15, the MEP surfaces visually represent these aspects. In this representation, the colors red, blue, and green correspond to negative, positive, and neutral zones, respectively. Particularly, the prominent negative red regions are situated between the nitrogen and oxygen atoms. This observation signifies a higher electron density and suggests the presence of potential nucleophilic sites within the molecule. On the other hand, the positive red regions are centered around the acidic hydrogen of the alcohol functional group.

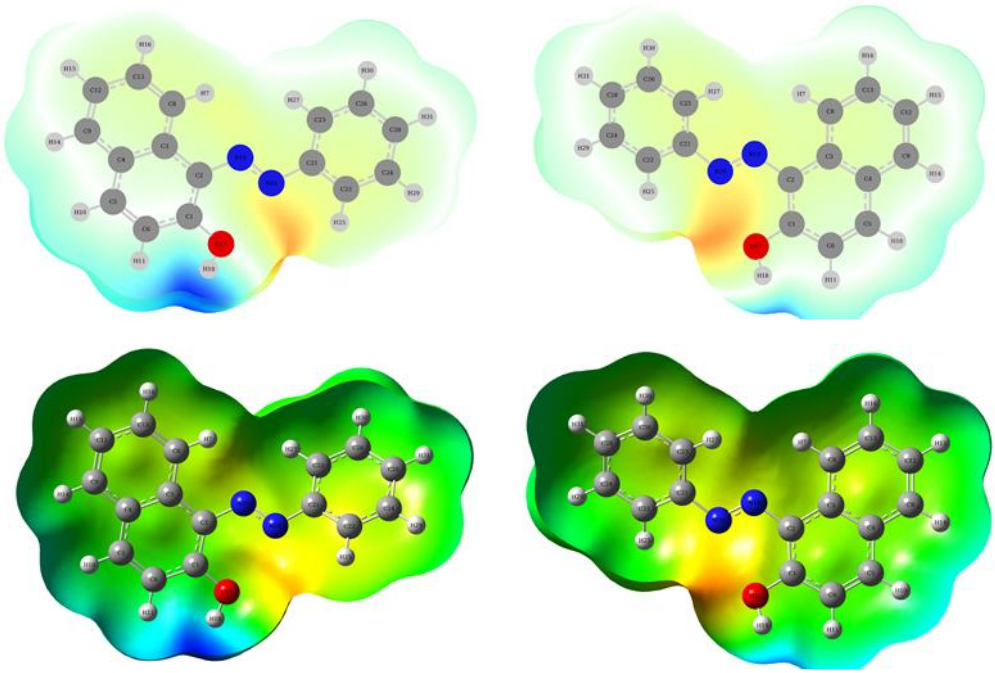

Figure 15. Molecular Electrostatic Potential (MEP) maps for the EPNO.

3.6.2.3. Global reactivity descriptors

The E_{HOMO} and E_{LUMO} values offer insights into the interaction between the inhibitor molecule and the metal surface, indicating donor-acceptor interactions. The effectiveness of the inhibitor molecule in corrosion inhibition tends to improve when the E_{HOMO} becomes less negative and the E_{LUMO} becomes more negative. This indicates that the molecule becomes more proficient at both donating and accepting electrons from the metal surface, a pivotal aspect for its role as a corrosion inhibitor. As evident from the data in Table 7, the form A of the EPNO molecule exhibits a substantial E_{HOMO} value (–5.9084 eV in aqueous phase and –5.7133 eV in gas phase) and a comparatively low E_{LUMO} value (–2.6161 eV in aqueous phase and –2.3655 eV in gas phase). This suggests its simultaneous capability to donate and accept electrons effectively.

The energy gap (ΔE), which denotes the difference in energy between the E_{HOMO} and E_{LUMO}, assumes a vital role in calculating various molecular attributes, encompassing optical and electronic properties, molecular stability, and notably, the reactivity of the inhibitor molecule during its adsorption onto a metal surface. Assessing chemical reactivity is essential for evaluating the effectiveness and structure of new inhibitors. The optimization and analysis of the HOMO–LUMO energy gap, coupled with other descriptors, yield valuable insights. A larger energy gap ΔE signifies heightened kinetic stability, decreased polarizability, and reduced reactivity for the EPNO molecule (3.2923 eV in aqueous phase and 3.3478 eV in gas phase). Accordingly, as ΔE diminishes, the corrosion inhibition performance strengthens. A smaller energy gap, therefore, corresponds to an amplified efficacy in corrosion inhibition. An inhibitor showcasing a higher hardness (η) value exhibits

a greater propensity for interaction with the metal surface. The η value correlates with the inhibitor molecule's polarizability, with a larger η indicating higher polarizability and an augmented likelihood of interaction with the metal surface. In contrast, inhibitors with lower η values exhibit a reduced inclination to engage with the metal surface. Based on the conclusions established in previous research [61, 68, 69], it can be deduced that the hardness of the studied inhibitor molecule falls within favorable ranges (η = 1.6462 eV in aqueous phase and 1.6739 eV in gas phase). This signifies that the EPNO molecule possesses promising anti-corrosive attributes and holds potential for effectively inhibiting corrosion of Fe-metal. These findings underscore the promise of the EPNO molecule as a corrosion inhibitor.

Table 7. Optimization energies, HOMO and LUMO energies and their gap calculated in gas phase at B3LYP/6-31+G(d,p) level of DFT calculations.

Descriptor	DFT	
	Gas phase	Aqueous phase
E_{HOMO} (eV)	–5.7133	–5.9084
E_{LUMO} (eV)	–2.3655	–2.6161
ΔE (eV)	3.3478	3.2923
I (eV)	5.7133	5.9084
A (eV)	2.3655	2.6161
χ (eV)	4.0394	4.2623
η (eV)	1.6739	1.6462
ΔN	0.2332	0.1694

The electronegativity (χ) of a molecule serves as an indicator of its electron-attracting ability. A higher χ value indicates a stronger electron-attracting influence, while a lower χ value suggests an increased predisposition to donate electrons with ease. In the context of the EPNO molecule, possessing a lower χ value (χ = 4.2623 eV in aqueous phase and 4.0394 eV in gas phase), it becomes apparent that EPNO interacts more favorably with the metal surface, especially when the metal surface, such as iron (χ_{Fe} = 4.820 eV), carries a higher electronegativity value. This indicates that the EPNO molecule can readily donate electrons to the metal surface, further enhancing its potential as an effective corrosion inhibitor.

3.6.3. MD and MC modelling results

Molecular simulations MC and MD were used to gain a molecular understanding of the adsorption behavior of EPNO/$EPNOH^+$ in the corrosive media onto the Fe-surface [35, 70]. The top views of final lowest energy configurations of neutral and protonated (*i.e.*

EPNO/EPNOH$^+$) title molecule above Fe-substrate derived from MD and MC simulations are shown in Figure 16.

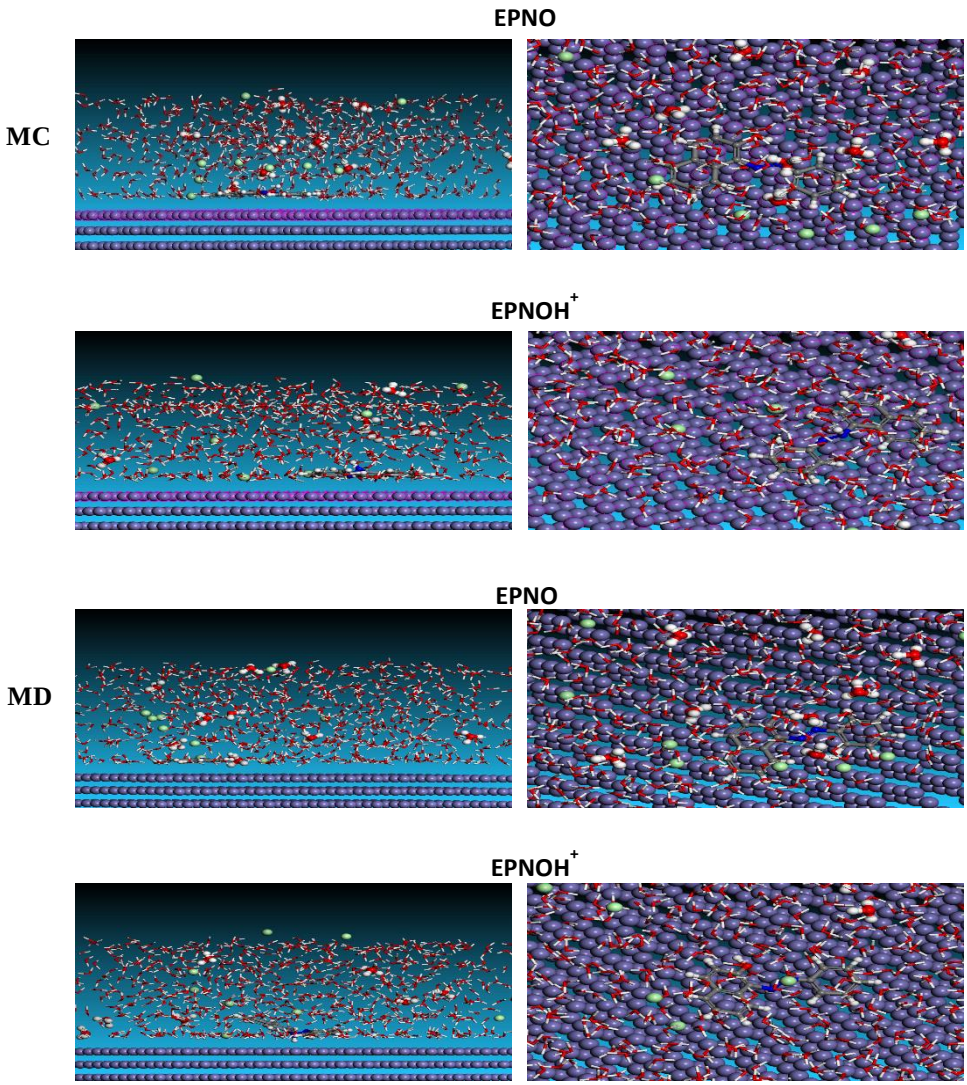

Figure 16. The final snapshots of EPNO and EPNOH$^+$ over Fe-surface obtained from MD and MC simulations.

These equilibrated snapshots show that the proposed corrosion inhibitor in neutral and protonated forms is adsorbed on the Fe-surface with its molecular skeleton containing the O and N atoms aligned planarly to the surface. These atoms serve as reactive sites for the inhibitor's interaction with the Fe-surface [71]. Corrosion inhibitors prevent corrosion by adsorbing on the metal surface through accepting electrons from the metal surface and by electron donation *via* its heteroatoms/C=C bonds. Moreover, the two structures EPNO/EPNOH$^+$ of the title molecule seem to take the place of water (H_2O) molecules and H_3O^+/Cl^- ions in a corrosive medium and provide a more stable location on the Fe-surface. In addition, the aqueous solution binds to the group (N=NH$^+$) of the protonated form (EPNOH$^+$) creating an ion pair onto the Fe-surface, while this is not the case for neutral form

(EPNO). for the protonated form in the HCl medium, this could result in additional stability of the studied inhibitor as it approaches the iron (110) substrate. The adsorption energy distribution for the systems for Fe(110)/EPNO/1000H_2O/10H_3O^+/10Cl^- and Fe(110)/EPNOH$^+$/1000H_2O/10H_3O^+/10Cl^- interfaces obtained by MC simulation are presented in Figure 17.

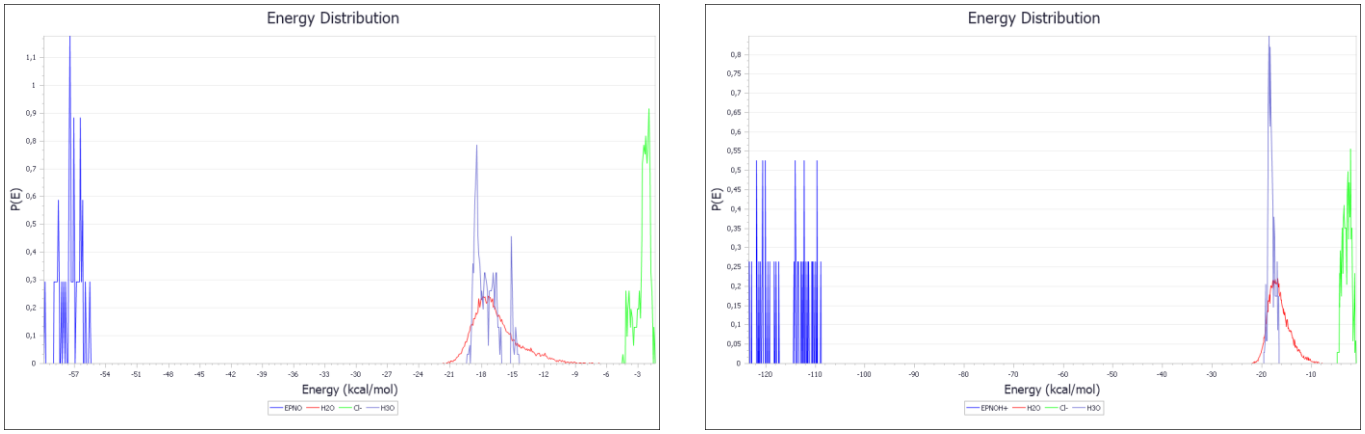

Figure 17. Adsorption energy distribution for the (Fe(110)/EPNO/1000H_2O/10H_3O^+/10Cl^- and Fe(110)/EPNOH$^+$ 1000H_2O/10H_3O^+/10Cl^-) systems obtained by the MC simulations.

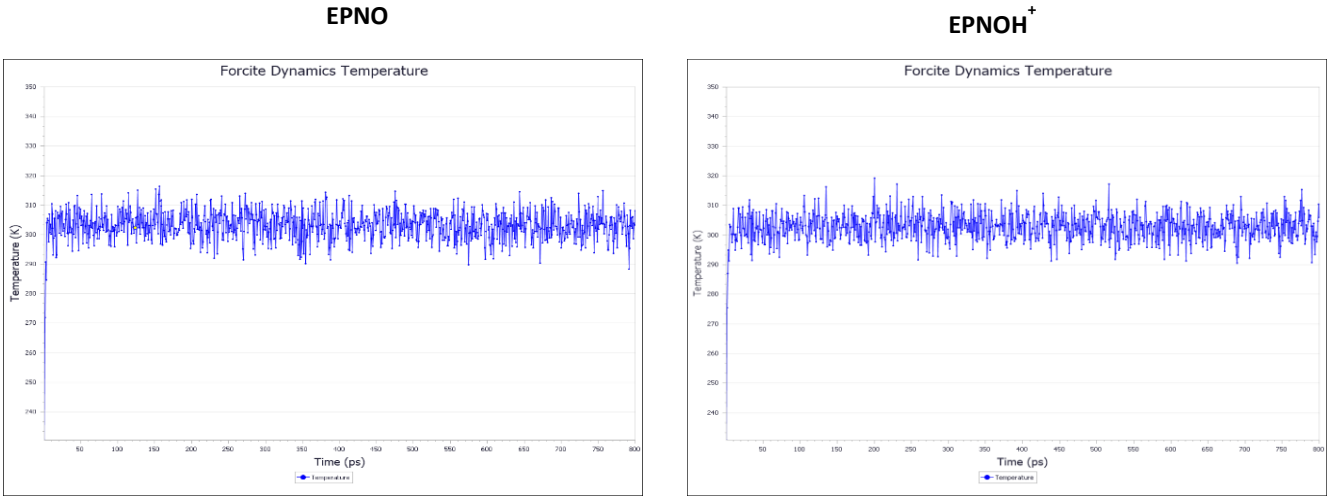

Figure 18. Temperature equilibrium curves for (Fe(110)/EPNO/1000H_2O/10H_3O^+/10Cl^- and Fe(110)/EPNOH$^+$ 1000H_2O/10H_3O^+/10Cl^-) systems.

In general, a more negative value of the adsorption energy (E_{ads}) indicates stronger and more spontaneous interactions between the inhibitor compound and the metal surface [72]. As shown in Figure 17, the adsorption energy of EPNOH$^+$ reaches (–123 kcal/mol), than that of EPNO, which is closer to (–60 kcal/mol), which shows the adsorption stronger for EPNOH$^+$ and EPNO, with a preference for EPNOH$^+$. MD simulations can track and study the kinetics of inhibitor adsorption on metal surfaces. Monitoring any temperature changes that occur throughout the MD simulation run is one method for ensuring that the components

contain the least amount of energy possible. The temperature distribution generated by MD simulation should be limited to 5 to 15% for an equilibrium interface under a particular temperature requirement [73]. based on the temperature graphs for ($Fe(110)/EPNO/1000H_2O/10H_3O^+/10Cl^-$ and $Fe(110)/EPNOH^+/1000H_2O/10H_3O^+/10Cl^-$) systemes calculated by MD at 303 K (Figure 18).

The minor temperature variations during the MD simulation suggest that the run was successful, which means that all systems have attained their equilibrium states. The different types of energetic descriptors of adsorbed EPNO and $EPNOH^+$ in the aqueous phase are calculated and listed in Table 8. It is significant to mention that the higher and negative values of adsorption energy (E_{ads}) indicates stable/easier adsorption onto the Fe(110) surface, as well as higher inhibition efficiency. From the Table 8, it is clear that the E_{ads} of EPNO is closer to –5575.01 kcal/mol than that of $EPNOH^+$, which is closer to –5615.59 kcal/mol, indicating that the title molecule ($EPNO/EPNOH^+$) in solution phases interacts strongly with the iron-based layer and then forming a protective adsorbed film with a preference for $EPNOH^+$.

Table 8. MC simulations descriptors for the adsorption of $EPNO/EPNOH^+$ in aqueous phases over the Fe(110) surface at 303 K (all values in kcal/mol).

System	E_{tot}	E_{ads}	E_{RA}	E_{def}	dE_{ads}/dN_{iinhib}	dE_{ads}/dN_{iH2O}	dE_{ads}/dN_{iH3O^+}	dE_{ads}/dN_{iCl^-}
Aqueous phase								
$Fe(110)/EPNO/1000H_2O/10H_3O^+/10Cl^-$	–4638.03	–5575.01	–4786.74	–788.27	–58.24	–8.24	–14.73	–1.93
$Fe(110)/EPNOH^+/1000H_2O/10H_3O^+/10Cl^-$	–4627.14	–5615.59	–4773.02	–842.57	–117.30	–9.91	–16.87	–1.91

Additionally, the type of bonds (*i.e*. physical, chemical, or both) generated between $EPNO/EPNOH^+$ structures and iron atoms are determined using the radial distribution function (RDF) approach. If the bond length value is between 1–3.5 Å, chemisorption is generally used, whereas physisorption (Van der Waals and Coulomb interactions) is normally used when the bond length value is greater than 3.5 Å [74, 75]. Figure 19 shows the radial distribution function of the $EPNO/EPNOH^+$ by MD trajectory.

As illustrated in Figure 19, all of the first peak values for $EPNO/EPNOH^+$ in solution phases are less than 3.5 Å (chemisorption range). These are the most critical interactions of the title molecule's modelled structures on Fe-surface, demonstrating that the title molecule does indeed inhibit the disintegration of the tested metal.

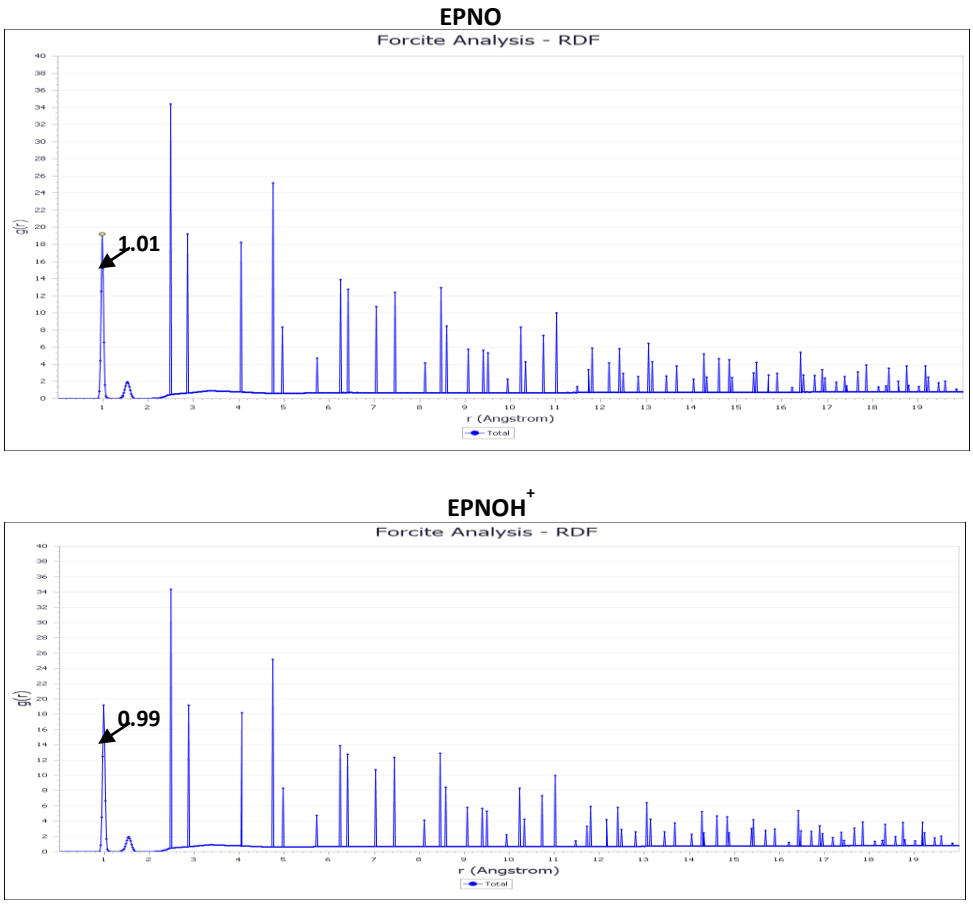

Figure 19. RDF of the EPNO/EPNOH$^+$ on the Fe-surface in corrosive medium.

4. Conclusions

Through the investigation carried on EPNO inhibitive potential for CS in 1 M HCl medium, multiple interesting outcomes can be drawn:

- Electrochemical techniques revealed that EPNO has excellent potency to mitigate corrosion of CS in 1 M HCl.
- PDP plots showed that EPNO can be regarded as a mixed type inhibitor.
- The adsorption process of EPNO obeyed to Langmuir's model.
- SEM micrographs depicted a good coverage of CS surface by EPNO adsorbed protective layer.
- UV-visibe trials validated the chemical interaction between EPNO and CS surface.
- The outcomes are notably consistent with DFT calculations, revealing a good correlation between the molecular structure of EPNO and its efficiency as an inhibitor. The amalgamation of experimental and computational analyses has led to the identification of a novel and efficient corrosion inhibitor for mild steel in a 1 M HCl solution.

References

1. A. Alazizi, A. Draskovics, G. Ramirez, A. Erdemir and S.H. Kim, Tribochemistry of carbon films in oxygen and humid environments: oxidative wear and galvanic corrosion, *Langmuir*, 2016, **32**, 1996–2004. doi: 10.1021/acs.langmuir.5b04207
2. Y. Ma, Y. Li and F. Wang, Corrosion of low carbon steel in atmospheric environments of different chloride content, *Corros. Sci*., 2009, **51**, 997–1006. doi: 10.1016/j.corsci.2009.02.009
3. M. Abbas and M. Shafiee, An overview of maintenance management strategies for corroded steel structures in extreme marine environments, *Mar. Struct*., 2020, **71**, 102718. doi: 10.1016/j.marstruc.2020.102718
4. S. Abdulhadi, A. Mohammed, W.K. Al-Azzawi, T. Gaaz, A.A.H. Kadhum, L.M. Shaker and A.A. Al-Amiery, The corrosion inhibition abilities of PVA and PVP against the corrosion of mild steel in hydrochloric acid, *Int. J. Corros. Scale Inhib*., 2023, **12**, no. 2, 645–663. doi: 10.17675/2305-6894-2023-12-2-14
5. I. Ahamad, R. Prasad and M.A. Quraishi, Inhibition of mild steel corrosion in acid solution by Pheniramine drug: experimental and theoretical study, *Corros. Sci*., 2010, **52**, 3033–3041. doi: 10.1016/j.corsci.2010.05.022
6. X. Su, C. Lai, L. Peng, H. Zhu, L. Zhou, W. Zhang, L. Zhang and X. Liu, A Dialkyldithiophosphate Derivative as Mild Steel Corrosion Inhibitor in Sulfuric Acid Solution, *Int. J. Electrochem. Sci*., 2016, **11**, 4828–4839. doi: 10.20964/2016.06.45
7. A. Gangan, M. ElSabbagh, M. Bedair, M. El-Sabbah and A. Fahmy, Plasma power impact on electrochemical performance of low carbon steel coated by plasma thin teos films, *Al-Azhar Bull. Sci*., 2020, **31**, 51–58. doi: 10.21608/absb.2020.111474
8. A.A. Baba, F.A. Adekola and A.O. Folashade, Quantitative leaching of a Nigerian iron ore in hydrochloric acid, *J. Appl. Sci. Environ. Manage*., 2005, **9**, no. 3, 15–20. doi: 10.4314/jasem.v9i3.17346
9. I.D. Amune, Investigation of Stress Corrosion Cracking of Storage Tanks used to Store Methanol for Gas Hydrate Inhibition, Doctoral dissertation, 2018.
10. A. Dehghani, G. Bahlakeh and B. Ramezanzadeh, A detailed electrochemical/theoretical exploration of the aqueous Chinese gooseberry fruit shell extract as a green and cheap corrosion inhibitor for mild steel in acidic solution, *J. Mol. Liq*., 2019, **282**, 366–384. doi: 10.1016/j.molliq.2019.03.011
11. G.D. Camila and F.G. Alexandre, Corrosion inhibitors–principles, mechanisms and applications, *Developments in corrosion protection*, IntechOpen, 2014, 365–379.
12. N. Benzbiria, A. Thoume, S. Echihi, M.E. Belghiti, A. Elmakssoudi, A. Zarrouk, M. Azzi and M. Zertoubi, Coupling of experimental and theoretical studies to apprehend the action of benzodiazepine derivative as a corrosion inhibitor of carbon steel in 1 M HCl, *J. Mol. Struct*., 2023, **1281**, 135139. doi: 10.1016/j.molstruc.2023.135139

13. W. Zhang, R. Ma, H. Liu, Y. Liu, S. Li and L. Niu, Electrochemical and surface analysis studies of 2-(quinolin-2-yl)quinazolin-4(3H)-one as corrosion inhibitor for Q235 steel in hydrochloric acid, *J. Mol. Liq*., 2016, **222**, 671–679. doi: 10.1016/j.molliq.2016.07.119
14. A. Suárez-Vega, C. Agustín-Sáenz, L.A. O'Dell, F. Brusciotti, A. Somers and M. Forsyth, Properties of hybrid sol-gel coatings with the incorporation of lanthanum 4-hydroxy cinnamate as corrosion inhibitor on carbon steel with different surface finishes, *Appl. Surf. Sci*., 2021, **561**, 149881. doi: 10.1016/j.apsusc.2021.149881
15. E.F. Olasehinde, B.E. Agbaffa, M.A. Adebayo and J. Enis, Corrosion protection of mild steel in acidic medium by titanium-based nanocomposite of *Chromolaena odorata* leaf extract, *Mater. Chem. Phys*., 2022, **281**, 125856. doi: 10.1016/j.matchemphys.2022.125856
16. C.A. Loto, R.T. Loto and A.P. Popoola, Performance evaluation of zinc anodes for cathodic protection of mild steel corrosion in HCl, *Chem. Data Collect*., 2019, **24**, 100280. doi: 10.1016/j.cdc.2019.100280
17. N. Mechbal, M.E. Belghiti, N. Benzbiria, C.H. Lai, Y. Kaddouri, Y. Karzazi, R. Touzani and M. Zertoubi, Correlation between corrosion inhibition efficiency in sulfuric acid medium and the molecular structures of two newly eco-friendly pyrazole derivatives on iron oxide surface, *J. Mol. Liq*., 2021, **331**, 115656. doi: 10.1016/j.molliq.2021.115656
18. A. Thoume, I.N. Irahal, N. Benzbiria, D.B. Left, R. Achagar, A. Elmakssoudi, A.A. El foulani, M. Dakir, M. Azzi, N. Bourhim and M. Zertoubi, *In vitro* and *in silico* antibacterial and anti-corrosive properties of *Persea americana* leaves extract as an environmentally friendly corrosion inhibitor for carbon steel in a Hydrochloric acid medium, *Colloids Surf., A*, 2023, **674**, 131848. doi: 10.1016/j.colsurfa.2023.131848
19. S. Echihi, N. Benzbiria, M. Beraich, M. Elfal, M. Elbelghiti, M. Boudalia, A. Bellaouchou, A. Guenbour, E. Mabrouk, D. Chebabe, M. Tabyaoui, I. Warad and A. Zarrouk, Experimental and theoretical investigation to the mild steel's corrosion inhibition using pyrazole pyrimidine derivative, *Chem. Data Collect*., 2023, **46**, 101049. doi: 10.1016/j.cdc.2023.101049
20. A.O. Alao, A.P. Popoola, M.O. Dada and O. Sanni, Utilization of green inhibitors as a sustainable corrosion control method for steel in petrochemical industries: A review, *Front. Energy Res*., 2023, **10**, 1063315. doi: 10.3389/fenrg.2022.1063315
21. S.S. Alarfaji, I.H. Ali, M.Z. Bani-Fwaz and M.A. Bedair, Synthesis and Assessment of Two Malonyl Dihydrazide Derivatives as Corrosion Inhibitors for Carbon Steel in Acidic Media: Experimental and Theoretical Studies, *Molecules*, 2021, **26**, no. 11, 3183. doi: 10.3390/molecules26113183
22. M.M. Abdelsalam, M.A. Bedair, A.M. Hassan, B.H. Heakal, A. Younis, Z.I. Elbialy, M. A. Badawy, H.E.-D. Fawzy and S.A. Fareed, Green synthesis, electrochemical, and DFT studies on the corrosion inhibition of steel by some novel triazole Schiff base derivatives in hydrochloric acid solution, *Arabian J. Chem*., 2022, **15**, 103491. doi: 10.1016/j.arabjc.2021.103491

23. M.A. Abbas, M.A. Bedair, O.E. El-Azabawy and E.S. Gad, Anticorrosion effect of ethoxylate sulfanilamide compounds on carbon steel in 1 M hydrochloric acid: electrochemical and theoretical studies, *ACS Omega*, 2021, **6**, no. 23, 15089–15102. doi: 10.1021/acsomega.1c01274
24. Y. Zhou, S. Xu, L. Guo, S. Zhang, H. Lu, Y. Gong and F. Gao, Evaluating two new Schiff bases synthesized on the inhibition of corrosion of copper in NaCl solutions, *RSC Adv*., 2015, **5**, 14804–14813. doi: 10.1039/C4RA14449J
25. N. Benzbiria, S. Echihi, M.E. Belghiti, A. Thoume, A. Elmakssoudi, A. Zarrouk, M. Zertoubi and M. Azzi, Novel synthetized benzodiazepine as efficient corrosion inhibitor for copper in 3.5% NaCl solution, *Mater. Today Proc*., 2021, **37**, 3932–3939. doi: 10.1016/j.matpr.2020.09.030
26. M.A. Frontini, W. Schreiner, M. Vázquez and M.B. Valcarce, Nitrite corrosion inhibition in chloride-rich electrolytes correlated to the electrical properties of surface films on carbon steel, *Constr. Build. Mater*., 2019, **227**, 116650. doi: 10.1016/j.conbuildmat.2019.08.031
27. W. Al Garadi, K. Jrajri, M. El Faydy, F. Benhiba, L. El Ghayati, N.K. Sebbar, E.M. Essassi, I. Warad, A. Guenbour, A. Bellaouchou, C. Jama, A. Alsalme and A. Zarrouk, 4-phenyl-decahydro-1*H*-1,5-benzodiazepin-2-one as novel and effective corrosion inhibitor for carbon steel in 1 M HCl solution: a combined experimental and empirical studies, J. Indian Chem. Soc., 2022, 100742. doi: 10.1016/j.jics.2022.100742
28. M.J. Frisch, G.W. Trucks, H.B. Schlegel, G.E. Scuseria, M.A. Robb, J.R. Cheeseman, G. Scalmani, V. Barone, G.A. Petersson, H. Nakatsuji, X. Li, M. Caricato, A. Marenich, J. Bloino, B.G. Janesko, R. Gomperts, B. Mennucci, H.P. Hratchian, J.V. Ortiz, A.F. Izmaylov, J.L. Sonnenberg, D. Williams-Young, F. Ding, F. Lipparini, F. Egidi, J. Goings, B. Peng, A. Petrone, T. Henderson, D. Ranasinghe, V.G. Zakrzewski, J. Gao, N. Rega, G. Zheng, W. Liang, M. Hada, M. Ehara, K. Toyota, R. Fukuda, J. Hasegawa, M. Ishida, T. Nakajima, Y. Honda, O. Kitao, H. Nakai, T. Vreven, K. Throssell, J.A. Montgomery, Jr., J.E. Peralta, F. Ogliaro, M. Bearpark, J.J. Heyd, E. Brothers, K.N. Kudin, V.N. Staroverov, T. Keith, R. Kobayashi, J. Normand, K. Raghavachari, A. Rendell, J.C. Burant, S.S. Iyengar, J. Tomasi, M. Cossi, J.M. Millam, M. Klene, C. Adamo, R. Cammi, J.W. Ochterski, R.L. Martin, K. Morokuma, O. Farkas, J.B. Foresman and D.J. Fox, *Gaussian 09, Revision E.01*, Gaussian, Inc., Wallingford CT, 2009.
29. A.D. Becke, Density-functional thermochemistry. III. The role of exact exchange, *J. Chem. Phys*., 1993, **98**, 5648–5652. doi: 10.1063/1.464913
30. C. Lee, W. Yang and R.G. Parr, Development of the Colle-Salvetti correlation-energy formula into a functional of the electron density, *Phys. Rev. B*, 1988, **37**, 785–789. doi: 10.1103/PhysRevB.37.785

31. G. Cinar, T. Agbektas, A. Huseynzada, G. Aliyeva, M. Aghayev, U. Hasanova, S. Kaya, S. Chtita, H. Nour, A. Tas and Y. Silig, Experimental and theoretical insights about the effect of some newly designed azomethine group-contained macroheterocycles on oxidative stress and DNA repair gene profiles in neuroblastoma cell lines, *J. Mol. Struct*., 2023, **1285**, 135432. doi: 10.1016/j.molstruc.2023.135432
32. T. Agbektas, C. Zontul, A. Ozturk, A. Huseynzada, R. Ganbarova, U. Hasanova, G. Cinar, A. Tas, S. Kaya, S. Chtita and Y. Silig, Effect of azomethine group containing compounds on gene profiles in Wnt and MAPK signal patterns in lung cancer cell line: *In silico* and *in vitro* analyses, *J. Mol. Struct*., 2023, **1275**, 134619. doi: 10.1016/j.molstruc.2022.134619
33. A.S. Mohamed, I. Jourdain, M. Knorr, A. Elmi, S. Chtita, R. Scheel, C. Strohmann and M.A. Hussien, Design of hydroxyl- and thioether-functionalized iron-platinum dimetallacyclopentenone complexes. Crystal and electronic structures, Hirshfeld and docking analyses and anticancer activity evaluated by *in silico* simulation, *J. Mol. Struct*., 2022, **1251**, 131979. doi: 10.1016/j.molstruc.2021.131979
34. A. Zahlou, S. Chtita, M. Ghamali, L. Bejjit, T. Lakhlifi and M. Bouachrine, Electronic and photovoltaic properties of new materials based on imidazo[1,2-a]pyrazine. Computational investigations, *Funct. Mater*., 2013, **20**, no. 4, 504–509. doi: 10.15407/fm20.04.504
35. N. Anusuya, J. Saranya, F. Benhiba, I. Warad, A. Zarrouk and S. Chitra, Isoxazoline Derivatives as Inhibitors for Mild Steel Corrosion in 1 M H_2SO_4: Computational and Experimental Investigations, *J. Mater. Eng. Perform*., 2022, **31**, 7204–7219. doi: 10.1007/s11665-022-06761-0
36. M. Abouchane, R. Hsissou, A. Molhi, M. Damej, K. Tassaoui, A. Berisha, A. Chraka and M. Benmessaoud, Exploratory Experiments Supported by Modeling Approaches for TGEEA New Epoxy Resin as a Contemporary Anti-corrosion Material for C38 Steel in 1.0 M HCl, *Failure Anal. Prev*., 2023, 1–17. doi: 10.1007/s11668-023-01705-9
37. H. Belcadi, A. Chraka, S. El Amrani, I. Raissouni, A. Moukhles, S. Zantar, L. Toukour and A.I. Mansour, Investigation and Valorization of the Moroccan *Salvia Officinalis* L. Essential Oil: Phytochemistry, Potential in Corrosion Inhibition, Antibacterial Activity, and Theoretical Modeling. *J. Bio- Tribo-Corros*., 2023, **9**, no. 3, 50. doi: 10.1007/s40735-023-00769-2
38. H. Sun, P. Ren and J. Fried, The COMPASS force field: parameterization and validation for phosphazenes, *Comput. Theor. Polym. Sci*., 1998, **8**, no. 1–2, 229–246. doi: 10.1016/S1089-3156(98)00042-7
39. A. Chraka, I. Raissouni, N.B. Seddik, S. Khayar, A.I. Mansour, S. Tazi, F. Chaouket and D. Bouchta, Identification of potential green inhibitors extracted from *Thymbra capitata* (L.) Cav. for the corrosion of Brass in 3% NaCl solution: experimental, SEM–EDX analysis, DFT computation and Monte Carlo simulation studies, *J. Bio- Tribo-Corros*., 2020, **6**, 1–19. doi: 10.1007/s40735-020-00377-4

40. A. Chraka, I. Raissouni, N.B. Seddik, S. Khayar, S. El Amrani, M. El Hadri, F. Chaouket and D. Bouchta, Croweacin and Ammi visnaga (L.) Lam Essential Oil derivatives as green corrosion inhibitors for brass in 3% NaCl medium: Quantum Mechanics investigation and Molecular Dynamics Simulation Approaches, *Mediterr. J. Chem*., 2020, **10**, 378. doi: 10.13171/mjc10402004281338ac
41. A.A. Al-Amiery, N. Betti, W.N.R.W. Isahak, W.K. Al-Azzawi and W.M.N. Wan Nik, Exploring the Effectiveness of Isatin – Schiff Base as an Environmentally Friendly Corrosion Inhibitor for Mild Steel in Hydrochloric Acid, *Lubricants*, 2023, **11**, no. 5, 211. doi: 10.3390/lubricants11050211
42. A. Chraka, N.B. Seddik, I. Raissouni, J. Kassout, M. Choukairi, M. Ezzaki, O. Zaraali, H. Belcadi, F. Janoub and A.I. Mansour, Electrochemical explorations, SEM/EDX analysis, and quantum mechanics/molecular simulations studies of sustainable corrosion inhibitors on the Cu-Zn alloy in 3% NaCl solution, *J. Mol. Liq*., 2023, **387**, 122715. doi: 10.1016/j.molliq.2023.122715
43. H. Derfouf, Y. Harek, L. Larabi, W.J. Basirun and M. Ladan, Corrosion inhibition activity of carbon steel in 1.0 M hydrochloric acid medium using hammada scoparia extract: gravimetric and electrochemical study, *J. Adhes. Sci. Technol*., 2019, **33**, no. 8, 808–833. doi: 10.1080/01694243.2018.1562321
44. X. Li, X. Xie, S. Deng and G. Du, Two phenylpyrimidine derivatives as new corrosion inhibitors for cold rolled steel in hydrochloric acid solution, *Corros. Sci*., 2014, **87**, 27–39. doi: 10.1016/j.corsci.2014.05.017
45. O.L. Riggs Jr, *Corrosion Inhibitors*, Second ed., C.C. Nathan, Houston, TX, 1973.
46. Y. El Ouadi, F. Abrigach, A. Bouyanzer, R. Touzani, O. Riant, B. ElMahi, A. El Assyry, S. Radi, A. Zarrouk and B. Hammouti, Corrosion inhibition of mild steel by new N-heterocyclic compound in 1 M HCl: Experimental and computational study, *Pharma Chem*., 2015, **7**, no. 8, 265–275.
47. Y.E. Louadi, F. Abrigach, A. Bouyanzer, R. Touzani, A. El Assyry, A. Zarrouk and B. Hammouti, Theoretical and Experimental Studies on the Corrosion Inhibition Potentials of Two Tetrakis Pyrazole Derivatives for Mild Steel in 1.0 M HCl, *Port. Electrochim. Acta*, 2017, **35**, no. 3, 159–178. doi: 10.4152/pea.201703159
48. M.A. Almomani, M.T. Hayajneh and M.W. AlSharman, *Ceratonia siliqua* pulp extracts as a green corrosion inhibitor for mild carbon steel in 1 M HCl, *Int. J. Corros. Scale Inhib*., 2023, **12**, no. 2, 793–810. doi: 10.17675/2305-6894-2023-12-2-23
49. Y.W. Liu, Y. Chen, X.H. Chen, Z.N. Yang and Z. Zhang, Study on adsorption behavior of ketoconazole on Q235 mild steel in 1.0 M HCl solution with electrochemical measurement, *J. Alloys Compd*., 2018, **758**, 184–193. doi: 10.1016/j.jallcom.2018.05.107
50. M. Goyal, H. Vashisht, S. Hamed Alrefaee, R. Jain, S. Kumar, S. Kaya, L. Guo and C. Verma, Decyltriphenylphosphonium bromide containing hydrophobic alkyl-chain as a potential corrosion inhibitor for mild steel in sulfuric acid: theoretical and experimental studies, *J. Mol. Liq*., 2021, **336**, 116166. doi: 10.1016/j.molliq.2021.116166

51. S. Cao, D. Liu, T. Wang, A. Ma, C. Liu, X. Zhuang, H. Ding, B.B. Mamba and J. Gui, Nitrogen-doped carbon dots as high-effective inhibitors for carbon steel in acidic medium, *Colloids Surf., A*, 2021, **616**, 126280. doi: 10.1016/j.colsurfa.2021.126280
52. D.K. Yadav, D.S. Chauhan, I. Ahamad and M.A. Quraishi, Electrochemical behavior of steel/acid interface: Adsorption and inhibition effect of oligomeric aniline, *RSC Adv*., 2013, **3**, no. 2, 632–646. doi: 10.1039/C2RA21697C
53. M. Kissi, M. Bouklah, B. Hammouti and M. Benkaddour, Establishment of equivalent circuits from electrochemical impedance spectroscopy study of corrosion inhibition of steel by pyrazine in sulphuric acidic solution, *Appl. Surf. Sci*., 2006, **252**, 4190–4197. doi: 10.1016/j.apsusc.2005.06.035
54. M. Zhang, L. Guo, M. Zhu, K. Wang, R. Zhang, Z. He, Y. Lin, S. Leng, V.C. Anadebe and X. Zheng, Akebia trifoliate koiaz peels extract as environmentally benign corrosion inhibitor for mild steel in HCl solutions: integrated experimental and theoretical investigations, *J. Ind. Eng. Chem*., 2021, **101**, 227–236. doi: 10.1016/j.jiec.2021.06.009
55. D.D. MacDonald, Review of mechanistic analysis by electrochemical impedance spectroscopy, *Electrochemical and Optical Techniques for the Study and Monitoring of Metallic Corrosion*, Dordrecht: Springer 203 (1991) 31–68. doi: 10.1007/978-94-011-3636-5_2
56. L.O. Olasunkanmi, N.I. Aniki, A.S. Adekunle, L.M. Durosinmi, S.S. Durodola, O.O. Wahab and E.E. Ebenso, Investigating the synergism of some hydrazinecarboxamides and iodide ions as corrosion inhibitor formulations for mild steel in hydrochloric Acid: experimental and computational studies, *J. Mol. Liq*., 2021, **343**, 117600. doi: 10.1016/j.molliq.2021.117600
57. E. Geler and D. Azambuja, Corrosion inhibition of copper in chloride solutions by pyrazole, *Corros. Sci*., 2000, **42**, no. 4, 631–643. doi: 10.1016/S0010-938X(99)00080-3
58. M.E. Belghiti, M. Mihit, A. Mahsoune, A. Elmelouky, R. Mghaiouini, A. Barhoumi, A. Dafali, M. Bakasse, M.A. El Mhammedi and M. Abdennouri, *J. Mater. Res. Technol*., 2019, **8**, no. 6, 6336–6353. doi: 10.1016/j.jmrt.2019.09.051
59. A. Thoume, D.B. Left, A. El Makssoudi, F. Benhiba, A. Zarrouk, N. Benzbiria, I. Warad, M. Dakir, M. Azzi and M. Zertoubi, Chalcone oxime derivatives as new inhibitors corrosion of carbon steel in 1 M HCl solution, *J. Mol. Liq*., 2021, **337**, 116398. doi: 10.1016/j.molliq.2021.116398
60. H.C. Andersen, Molecular dynamics simulations at constant pressure and/or temperature, *J. Chem. Phys*., 1980, **72**, 2384–2393. doi: 10.1063/1.439486
61. A. Zarrouk, B. Hammouti, H. Zarrok, S.S. Al-Deyab and M. Messali, Temperature effect, activation energies and thermodynamic adsorption studies of L-Cysteine methyl ester hydrochloride as copper corrosion inhibitor in nitric acid 2M, *Int. J. Electrochem. Sci*., 2011, **6**, 6261–6274. doi: 10.1016/S1452-3981(23)19679-9

62. M.E. Belghiti, S. Bouazama, S. Echihi, A. Mahsoune and A. Elmelouky, Understanding the adsorption of newly Benzylidene-aniline derivatives as a corrosion inhibitor for carbon steel in hydrochloric acid solution: experimental, DFT and molecular dynamic simulation studies, *Arabian J. Chem*., 2020, **13**, 1499–1519. doi: 10.1016/j.arabjc.2017.12.003
63. Y.K. Al-Majedy, H.H. Ibraheem, A.A. Issa and A. Alamiery, Exploring chromone derivatives as environmentally friendly corrosion inhibitors for mild steel in acidic environments: A comprehensive experimental and DFT study, *Int. J. Corros. Scale Inhib*., 2023, **12**, no. 3, 1028–1051. doi: 10.17675/2305-6894-2023-12-3-14
64. R. Nabah, F. Benhiba, Y. Ramli, M. Ouakki, M. Cherkaoui, H. Oudda, R. Touir, I. Warad and A. Zarrouk, Corrosion Inhibition Study of 5,5-diphenylimidazolidine-2,4-dione for Mild Steel Corrosion in 1 M HCl Solution: Experimental, Theoretical Computational and Monte Carlo Simulations Studies, *Anal. Bioanal. Electrochem*., 2018, **10**, no. 10, 1375–1398.
65. M.M. Solomon and S.A. Umoren, In-situ preparation, characterization and anticorrosion property of polypropylene glycol/silver nanoparticles composite for mild steel corrosion in acid solution, *J. Colloid Interface Sci*., 2016, **462**, 29–41. doi: 10.1016/j.jcis.2015.09.057
66. M. Rbaa, M. Fardioui, C. Verma, A.S. Abousalem, M. Galai, E.E. Ebenso, T. Guedira, B. Lakhrissi, I. Warad and A. Zarrouk, 8-Hydroxyquinoline based chitosan derived carbohydrate polymer as biodegradable and sustainable acid corrosion inhibitor for mild steel: experimental and computational analyses, *Int. J. Biol. Macromol*., 2020, **155**, 645–655. doi: 10.1016/j.ijbiomac.2020.03.200
67. S. Cao, D. Liu, P. Zhang, L. Yang, P. Yang, H. Lu and J. Gui, Green Bronsted acid ionic liquids as novel corrosion inhibitors for carbon steel in acidic medium, *Sci. Rep*. 2017, **7**, 8773. doi: 10.1038/s41598-017-07925-y
68. F. Benhiba, Z. Benzekri, Y. Kerroum, N. Timoudan, R. Hsissou, A. Guenbour, M. Belfaquir, S. Boukhris, A. Bellaouchou, H. Oudda and A. Zarrouk, Assessment of inhibitory behavior of ethyl 5-cyano-4-(furan-2-yl)-2-methyl-6-oxo-1,4,5,6-tetrahydropyridine-3-carboxylate as a corrosion inhibitor for carbon steel in molar HCl: Theoretical approaches and experimental investigation, *J. Indian Chem. Soc*., 2023, **100**, 100916. doi: 10.1016/j.jics.2023.100916
69. L. Afia, R. Salghi, A. Zarrouk, H. Zarrok, E.H. Bazzi, B. Hammouti and M. Zougagh, Comparative study of corrosion inhibition on mild steel in HCl Medium by three green compounds: *Argania spinosa* Press Cake, Kernels and Hulls Extracts, *Trans. Indian Inst. Met*., 2013, **66**, 43–49. doi: 10.1007/s12666-012-0168-z
70. H. Al-sharabi, K. Bouiti, F. Bouhlal, N. Labjar, G. Amine Benabdellah, A. Dahrouch, L. Hermouch, S. Kaya, B. El Ibrahimi, M. El Mahi, E.M. Lotfi, B. El Otmani and S. El Hajjaji, Anti-corrosive properties of *Catha Edulis* leaves extract on C38 steel in 1 M HCl media. Experimental and theoretical study, *Int. J. Corros. Scale Inhib*., 2022, **11**, no. 3, 956–984. doi: 10.17675/2305-6894-2022-11-3-4

71. I. Eliboev, E. Berdimurodov, K. Yakhshinorov, J. Abdisattarov, O. Dagdag, A. Berisha, W.W. Nik, A. Kholikov and K. Akbarov, Supramolecular corrosion protection: Eco-friendly synthesis and efficacy of a β-cyclodextrin/*o*-phenylenediamine complex, *J. Taiwan Inst. Chem. Eng*., 2023, **147**, 104944. doi: 10.1016/j.jtice.2023.104944
72. E. Ech-Chihbi, A. Nahlé, R. Salim, F. Benhiba, A. Moussaif, F. El-Hajjaji, H. Oudda, A. Guenbour, M. Taleb and I. Warad, *J. Alloys Compd*., 2020, **844**, 155842. doi: 10.1016/j.jallcom.2020.155842
73. M. Belhadi, M. Oubahou, I. Hammoudan, A. Chraka, M. Chafi and S. Tighadouini, A comprehensive assessment of carbon steel corrosion inhibition by 1,10-phenanthroline in the acidic environment: insights from experimental and computational studies, *Environ. Sci. Pollut. Res*., 2023, 1–18. doi: 10.1007/s11356-023-27582-1
74. V. Mehmeti and F.I. Podvorica, Experimental and theoretical studies on corrosion inhibition of niobium and tantalum surfaces by carboxylated graphene oxide, *Materials*, 2018, **11**, no. 6, 893. doi: 10.3390/ma11060893
75. H. Bouayadi, M. Damej, A. Molhi, Z. Lakbaibi, M. Benmessaoud and M. Cherkaoui, Electrochemical and theoretical evaluation of thiocarbohydrazide as a brass (60/40) corrosion inhibitor in 3% NaCl solution and effect of temperature on this process, *Int. J. Corros. Scale Inhib*., 2022, **11**, no. 3, 1335–1354. doi: 10.17675/2305-6894-2022-11-3-25

♦ ♦ ♦